OVERLAPPING DOMAIN DECOMPOSITION METHODS FOR PTYCHOGRAPHIC IMAGING

HUIBIN CHANG*, ROLAND GLOWINSKI†, STEFANO MARCHESINI‡, XUE-CHENG TAI§, YANG WANG¶, AND TIEYONG ZENG‖

Abstract. In ptychography experiments, redundant scanning is usually required to guarantee the stable recovery, such that a huge amount of frames are generated, and thus it poses a great demand of parallel computing in order to solve this large-scale inverse problem. In this paper, we propose the overlapping **D**omain **D**ecomposition **M**ethod**s** (DDMs) to solve the nonconvex optimization problem in ptychographic imaging. They decouple the problem defined on the whole domain into subproblems only defined on the subdomains with synchronizing information in the overlapping regions of these subdomains, thus leading to highly parallel algorithms with good load balance. More specifically, for the nonblind recovery (with known probe in advance), by enforcing the continuity of the overlapping regions for the image (sample), the nonlinear optimization model is established based on a novel **s**mooth-**t**runcated **a**mplitude-**G**aussian **m**etric (ST-AGM). Such metric allows for fast calculation of the proximal mapping with closed form, and meanwhile provides the possibility for the convergence guarantee of the first-order nonconvex optimization algorithm due to its Lipschitz smoothness. Then the **A**lternating **D**irection **M**ethod of **M**ultipliers (ADMM) is utilized to generate an efficient **O**verlapping **D**omain **D**ecomposition based **P**tychography algorithm (OD^{2}P) for the two-subdomain **d**omain **d**ecomposition (DD), where all subproblems can be computed with close-form solutions. Due to the Lipschitz continuity for the gradient of the objective function with ST-AGM, the convergence of the proposed OD^{2}P is derived under mild conditions. Moreover, it is extended to more general case including multiple-subdomain DD and blind recovery. Numerical experiments are further conducted to show the performance of proposed algorithms, demonstrating good convergence speed and robustness to the noise. Especially, we report the virtual wall-clock time of proposed algorithm up to 10 processors, which shows potential for upcoming massively parallel computations.

Key words. Overlapping domain decomposition method; Ptychography; Phase retrieval; Parallel computing; Smooth truncated amplitude-Gaussian metric; Blind recovery

AMS subject classifications. 46N10, 49N30, 49N45, 65F22, 65N21

1. Introduction.

X-ray ptychography [32] enables imaging with the large field of view and nano-scale resolution, by combining the technique of coherent diffraction imaging and scanning transmission X-ray microscopy. It has been applied to vast research areas, that helps to reveal the structures and chemical contrast of nano-scale materials. Thus it is very meaningful to develop efficient algorithms for ptychographic imaging. As a special case for the phase retrieval problem (the inverse quadratic problem) arising in wide areas including optics, crystallography, materials sciences etc., various algorithms developed in [28, 33] and references therein can be exploited to tackle this problem. Especially, for ptychography, recent algorithms [9, 32, 18, 34, 27, 36, 30, 20, 5, 12] have been developed in order to further improve the performance and work in various settings, e.g. partial coherence [4] and blind recovery [34, 27] for unknown probe.

As an important property of ptychography, a huge amount of the frames are usually collected such that the iterative imaging algorithms usually requires a large memory footprint and high computational cost. Therefore, it poses a great demand to develop parallel algorithms [31, 19, 29, 11]. Namely, the asynchronous parallel algorithm [31] was performed on partitions of entire dataset asynchronously to get the sub-images, and then merge these sub-images to the whole image. However, due to possible drifts and phase ambiguities (linear phase ambiguity [17] for blind recovery) for the recovered sub-images, high computation cost was required for pairwise registration and correction of phase ambiguities. To further improve the asynchronous algorithm, the authors [19, 31] also provided synchronous parallel algorithms, where either the boundary layers of the sub-images were synchronized by averaging all local neighborhood [31], or the entire image and probe were shared across all subdomains [19, 29]. Hybrid parallel combined with the alternating projection algorithm was implemented on GPU workstation [11], and similarly to [19, 29], each subdomain has the individual copy of the whole image and probe leading to high communication cost.

Domain decomposition methods (DDMs) have played a great role in solving partial differential equations

*Corresponding author. School of Mathematical Sciences, Tianjin Normal University, Tianjin, China, E-mail:changhuibin@gmail.com

†Department of Mathematics, University of Houston, Houston, USA

‡Computational Research Division, Lawrence Berkeley National Laboratory, Berkeley, USA

§Department of Mathematics, Hong Kong Baptist University, Kowloon Tong, Hong Kong

¶Department of Mathematics, The Hong Kong University of Science and Technology, Kowloon, Hong Kong

‖Department of Mathematics, The Chinese University of Hong Kong, Hong Kong

numerically [26, 3, 16]. Particularly, it allows for highly parallel computing with good load balance, by decomposing the equations on whole domain to the problems on relatively small subdomains with information synchronization on the partition interfaces. It has also been successfully extended to large-scale image restoration, image reconstruction and other inverse problems, e.g. [38, 13, 7, 22, 24, 21, 23, 25, 10, 35] and references therein. To the best of our knowledge, most of existing studies focused on the linear inverse problems with convex minimization modeling. In this paper, we will explore the potential using DDMs to realize parallel computing for ptychographic imaging, which essentially corresponds to a nonconvex quadratic inverse problem.

However, it seems quite difficult to design corresponding DDMs for the ptychographic imaging. On one hand, the forward operator for ptychography involves the Fourier transform (integral operator) of the multiplication of the probe and sliding patch of the image, such that direct non-overlapping decomposition of the image into subdomains cannot split the measured frames completely, leading to both high computational and communication cost (see a related work of the DDM for nonlocal operator [8]). On the other hand, there is lack of convergence studies of DDMs for nonconvex minimization problems. Especially, the convergence for the related first-order operator splitting algorithms seems difficult to guarantee, since the convention objective function [30, 6] is nonsmooth, and the smoothed version [5] based operator-splitting algorithm cannot get rid of additional inner loop.

We aim to design more efficient DDMs for ptychographic imaging with convergence guarantee. Simply one can see that the non-overlapping domain decomposition (DD) of the image (sample) cannot reduce both the computation and communication costs compared to the overlapping DD due to the Fourier transform. Therefore, we will consider the overlapping DD motivated by the overlapping scan style of ptychography experiments, such that the decomposed frames on the subdomains are completely decoupled. By enforcing the continuity of the image on joint layers of overlapping subdomains, we propose the **O**verlapping **DD** based **P**tychography algorithm (OD^{2}P) in the case of two-subdomain DD, utilizing the Alternating Direction Methods of Multipliers (ADMM [15, 37, 2]) in order to solve the constraint optimization problem with a modified metric. It is naturally extended to the case of the multiple-subdomain DD. As the size of the probe is much smaller than that of the image, the DDM for the blind recovery to recover the image and probe jointly is further proposed by sharing the joint probe across all subdomains, combined with the overlapping DD of the image. Comparing to the existing parallel imaging algorithms, there is no need to correct the phase ambiguity, and moreover, a clear mathematical framework is given with lower communication cost and strict theoretical convergence under quite mild conditions. The main contributions of this paper are summarized below:

- A novel smooth truncated metric is introduced to measure the recovered intensity and target, which allows for fast calculation of the proximal mapping with closed form, and meanwhile guarantees the convergence of the first-order optimization algorithm due to its Lipschitz smoothness.
- An overlapping DD is introduced to solve ptychography reconstruction, where a narrow layer of the whole sample is shared with adjacent subdomains. We further solve the ptychography model on the overlapping DD by using ADMM, which is essentially a fully splitting algorithm on the sense that all subproblems have closed-form solutions. Furthermore, with mild condition of the stepsizes, the convergence is derived. To the best of our knowledge, it is the first time to prove the convergence for DDMs in nonconvex problems.
- The DDMs are further extended to multiple-subdomain DD and blind recovery. For blind ptychography, we further propose a new variational model with the compact support set of Fourier transform of the probe, to get rid of grid pathology for grid scanning. Especially, we report the virtual wall-clock time of proposed algorithm for multiple DD, which shows high speedup efficiency up to 10 processors and potential for upcoming massively parallel computations.

The rest of paper is given below. In section 2, the proposed OD^{2}P based on the two-subdomain DD is presented for nonblind recovery with convergence guarantee under mild conditions of the stepsizes. It is further extended to the case of multiple-subdomain DD and blind recovery in section 3. Numerous experiments are conducted in section 4. Finally, conclusions and future work are given in section 5.

2. DDM for nonblind ptychography: Two-subdomain case. In a standard ptychography experiment, a localized coherent X-ray probe (or illumination) w scans through an image (or sample) u, while the detector collects a sequence of phaseless intensities in the far field. Throughout this paper, we consider the

following discrete setting. The variable $u \in \mathbb{C}^n$ (the complex Euclidean space) corresponds to a 2D image (sample) with $\sqrt{n}\times\sqrt{n}$ pixels, and $w \in \mathbb{C}^{\bar{m}}$ is a localized 2D probe with $\sqrt{\bar{m}}\times\sqrt{\bar{m}}$ pixels, where both u and w are written as a vector by a lexicographical order. A stack of phaseless measurements $\tilde{f}_j \in \mathbb{R}_+^{\bar{m}}\ \forall 0 \le j \le J-1$ ($\mathbb{R}_+^{\bar{m}}$ is the Euclidean space with non-negative elements) is collected with $\tilde{f}_j = |\mathcal{F}(w \circ \mathcal{S}_j u)|^2$, where notations $|\cdot|, ()^2$ represent the element-wise absolute, and square values of a vector respectively, $\circ$ denotes the element-wise multiplication, and $\mathcal{F}$ denotes the normalized discrete Fourier transformation. The operator $\mathcal{S}_j \in \mathbb{R}^{\bar{m}\times n}$ is denoted by a binary matrix that specifies a small window with the index j and size $\bar{m}$ over the entire image u. The general blind ptychography (BP) problem can then be expressed as follows:

$$\text{To find}\ \ w \in \mathbb{C}^{\bar{m}} \text{ and } u \in \mathbb{C}^n, \ \text{ such that } \ |\mathcal{F}(w \circ \mathcal{S}_j u)|^2 = \tilde{f}_j\ \forall 0 \le j \le J-1. \tag{2.1}$$

In this section, we assume that the probe w is known in advance. Denote the linear operator $A : \mathbb{C}^n \to \mathbb{C}^m$ ($m = J \times \bar{m}$) as $Au := \left((\mathcal{F}(w \circ \mathcal{S}_0 u))^T, (\mathcal{F}(w \circ \mathcal{S}_1 u))^T, \cdots, (\mathcal{F}(w \circ \mathcal{S}_{J-1} u))^T\right)^T \ \ \forall\ u \in \mathbb{C}^n$, such that the nonblind ptychography reconstruction can be modeled below:

$$\text{To find the image } u \in \mathbb{C}^n, \ \text{ s.t. } \ |Au|^2 = f, \tag{2.2}$$

with the phaseless data $f := (\tilde{f}_0^T, \tilde{f}_1^T, \cdots, \tilde{f}_{J-1}^T)^T \in \mathbb{R}^m$ and the given probe w.

2.1. Overlapping domain decomposition. Denote the whole region $\Omega := \{0, 1, 2, \cdots, n-1\}$ in the discrete setting. There exists the two-subdomain overlapping DD $\{\Omega_d\}_{d=1}^2$, such that $\Omega = \bigcup_{d=1}^2 \Omega_d$ with $\Omega_d := \{l_0^d, l_1^d, \cdots, l_{n_d-1}^d\}$, and the overlapping region is denoted as $\Omega_{1,2} := \Omega_1 \cap \Omega_2 = \{\hat{l}_0, \hat{l}_1, \cdots, \hat{l}_{\hat{n}-1}\}$. Here we consider a special overlapping DD. As shown in Fig. 1 (b) (totally 4×4 frames) for grid scan, each subdomain contains a complete scanning frame, i.e. the right (or left) boundaries of frames near the left(or right) subdomain interface lies exactly on the right(or left) boundary of subdomains. Denote the restriction operators R_1, R_2 as $R_d u = u|_{\Omega_d}$ and $R_{1,2} u = u|_{\Omega_{1,2}}$, i.e. $(R_d u)(j) = u(l_j^d) \forall\ 0 \le j \le n_d - 1$, $(R_{1,2} u)(j) = u(\hat{l}_j) \forall 0 \le j \le \hat{n} - 1$. Then two groups of localized shift operators can be introduced $\{\mathcal{S}_{j_d}^d\}_{j_d=0}^{J_d-1}, d = 1, 2$, with $\sum_d J_d = J$. Therefore, we can denote the linear operators A_1, A_2 on the subdomains as

$$A_d u_d := \left((\mathcal{F}(w \circ \mathcal{S}_0^d u_d))^T, (\mathcal{F}(w \circ \mathcal{S}_1^d u_d))\right)^T, \cdots, (\mathcal{F}(w \circ \mathcal{S}_{J_d-1}^d u_d))^T)^T \ \ d = 1, 2. \tag{2.3}$$

Naturally, the measurement f is also decomposed to two non-overlapping parts f_1, f_2, i.e. $f_d := |A_d R_d u|^2$ assuming that (u, f) follows (2.2).

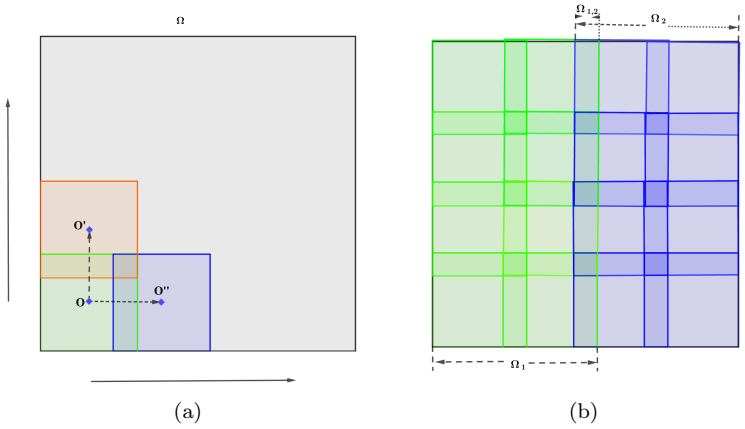

FIG. 1. *(a) Ptychography scan in the domain Ω (grid scan): the starting scan centers at point* **O**, *and then move up (or to the right) with the center point* **O'** *(or* **O"** *); (b) Two-subdomain DD (totally 4×4 frames): The subdomains Ω_1, Ω_2 are generated by two 4×2-scans, and the overlapping region $\Omega_{1,2} = \Omega_1 \cap \Omega_2$.*

We remark that as shown in Fig. 1, the width of the overlapping region $\Omega_{1,2}$ is $\sqrt{\bar{m}} - n_{stepsize}$, with the scan stepsize $n_{stepsize}$ pixels (assuming the stepsizes are same for $x, y-$directions). Therefore, letting the stepsize $n_{stepsize} < \sqrt{\bar{m}}$ guarantees the sufficient overlap of the two-subdomain DD, that immediately

demonstrates that sufficient redundancy of the scan for ptychography leads to enough overlap of the DD. We also remark that one can first divide the measurements with non-overlapping partitions as shown in Fig. 1 (b), that will automatically generate the overlapping DD.

2.2. A new nonlinear optimization model. For simplicity, we consider the decomposition with only two subdomains, and rewrite the problem (2.2) on the whole region to the following equations

$$|A_1 u_1|^2 = f_1, \quad |A_2 u_2|^2 = f_2, \tag{2.4}$$

with the continuity of the overlapping regions

$$\pi_{1,2} u_1 = \pi_{2,1} u_2, \tag{2.5}$$

where the operators $\pi_{1,2}$ (restriction from Ω_1 into $\Omega_{1,2}$) and $\pi_{2,1}$ (restriction from Ω_2 into $\Omega_{1,2}$) are denoted as $\pi_{1,2}u_1 := R_{1,2}R_1^T u_1$, and $\pi_{2,1}u_2 := R_{1,2}R_2^T u_2$. Remarkably, the continuity condition is essential for the perfect reconstruction of the ptychography. Without this condition, the redundancy of the boundary layer may not be sufficient such that there will be visible artifacts in the final reconstruction results and meanwhile phase ambiguities need to be corrected.

We will discuss how to solve the above problem efficiently. One may solve the problem using a Schwarz alternating method [26]. However, directly solving this multivariable quadratic system is generally NP-complete. Alternatively, we seek the solution by nonlinear optimization. With the popular amplitude-Gaussian metric (AGM) [36, 12] to measure the fitting errors, one can readily establish the following nonlinear optimization model

$$\min_{u_1,u_2} \sum_{d=1}^{2} \tfrac{1}{2} \left(\left\| |A_d u_d| - \sqrt{f_d} \right\|^2 \right), \quad s.t.\ \pi_{1,2} u_1 = \pi_{2,1} u_2,$$

where $\sqrt{\cdot}$ denotes the element-wise square root of a vector, and $\|\cdot\|$ denotes the standard ℓ^2 norm in real or complex Euclidean space. Due to lack of smoothness, one may introduce a modified metric [18, 5, 14] with additional penalization factor in order to gain the convergence guarantee. However, an inner loop has to be introduced [5], since the proximal mapping of the modified metric does not have closed form solution.

Readily one sees that the AGM is smooth except at the origin. Instead of smoothing the function by adding a global penalization factor [18, 5, 14], a more simple but effective way is to cut off the AGM near the origin, and then add back a smooth function which can keep the global minimizer unchanged. At the same time, it should not increase computational cost compared with AGM. Hence, a novel smooth truncated AGM (ST-AGM) $\mathcal{G}_\epsilon(\cdot; f)$ with truncation parameter $\epsilon > 0$ is designed below:

$$\mathcal{G}_\epsilon(z; f) := \sum\nolimits_j g_\epsilon(z(j); f(j)), \tag{2.6}$$

where $\forall \ \ x \in \mathbb{C}, b \in \mathbb{R}^+$,

$$g_\epsilon(x; b) := \begin{cases} \dfrac{1-\epsilon}{2} \left(b - \tfrac{1}{\epsilon}|x|^2 \right), & \text{if } |x| < \epsilon\sqrt{b}; \\ \dfrac{1}{2} \left| |x| - \sqrt{b} \right|^2, & \text{otherwise.} \end{cases} \tag{2.7}$$

One readily sees that the new metric is a mixture of the AGM and a quadratic function (smooth connected). Please also see Fig. 2 for the landscape of ST-AGM in 1-dimension: Among four different plots with $\epsilon = 0, 0.1, 0.5, 1.5$, one can observe that the minimizer does not change w.r.t. different ϵ $(0 \le \epsilon < 1)$; However, if $\epsilon > 1$, the global minimizer moves to the origin. Hence, to keep the minimizer unchanged, we set $\epsilon \in (0, 1)$ hereafter.

Denote the corresponding proximal mapping of g_ϵ as $\text{Prox}_{\mathcal{G}_\epsilon;\lambda}(y) := \arg\min_z \mathcal{G}_\epsilon(z; f) + \frac{\lambda}{2}\|z - y\|^2$. After simple calculations, one derives the following closed form solution with $\epsilon \in (0, 1)$:

$$(\text{Prox}_{\mathcal{G}_\epsilon;\lambda}(y))(j) = \text{sign}(y(j)) \times \begin{cases} \max\left\{0, \frac{\lambda|y(j)|}{\lambda - \frac{1-\epsilon}{\epsilon}}\right\}, & \text{if } |y(j)| < \epsilon - \frac{1-\epsilon}{\lambda}\sqrt{f(j)}; \\ \frac{\sqrt{f(j)} + \lambda|y(j)|}{1+\lambda}, & \text{otherwise.} \end{cases} \tag{2.8}$$

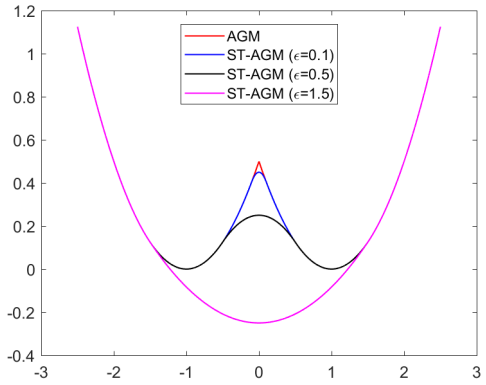

FIG. 2. *Landscapes of ST-AGM as* $g_\epsilon(x,1)$ $\forall x \in \mathbb{R}$ *(*$\epsilon = 0, 0.1, 0.5, 1.5$*). If* $\epsilon = 0$*, ST-AGM is exactly the same as AGM.*

One can further show that $\mathcal{G}_\epsilon(z;f)$ is Lipschitz differentiable by the following lemma.

Lemma 2.1. *Denote* $L := \frac{2}{\epsilon} - 1$*. The function* $\mathcal{G}_\epsilon(\cdot;f)$ *is Lipschitz differentiable, i.e.*

$$\|\nabla_z \mathcal{G}_\epsilon(z;f) - \nabla_z \mathcal{G}_\epsilon(y;f)\| \le L\|z-y\| \quad \forall\ z,y \in \mathbb{C}^m. \tag{2.9}$$

Proof. We will show the Lipschitz continuity of $\nabla_x g_\epsilon(\cdot;b)$. Denoting $\mathcal{K}_1 := \{x \in \mathbb{C} :\ |x| < \epsilon\sqrt{b}\}$ and $\mathcal{K}_2 := \mathbb{C} \setminus \mathcal{K}_1$. Readily one knows that $g_\epsilon(x;b) \in \mathcal{C}^1$ if $\epsilon > 0$, where the gradient is given below

$$\nabla_x g_\epsilon(x;b) = \begin{cases} (1-\frac{1}{\epsilon})x, & \text{if } x \in \mathcal{K}_1; \\ (1-\frac{\sqrt{b}}{|x|})x, & \text{otherwise.} \end{cases} \tag{2.10}$$

It is not difficult to see that

$$|\nabla_x g_\epsilon(x_1;b) - \nabla_x g_\epsilon(x_2;b)| = |\tfrac{1}{\epsilon} - 1|\ |x_1 - x_2| \quad \forall x_1, x_2 \in \mathcal{K}_1. \tag{2.11}$$

One can also get

$$\begin{aligned} &|\nabla_x g_\epsilon(x_1;b) - \nabla_x g_\epsilon(x_2;b)| \le |(1-\tfrac{\sqrt{b}}{|x_1|})(x_1-x_2)| + |(\tfrac{\sqrt{b}}{|x_1|} - \tfrac{\sqrt{b}}{|x_2|})x_2| \\ \le &|1-\tfrac{\sqrt{b}}{|x_1|}|\ |x_1-x_2| + \tfrac{\sqrt{b}}{|x_1|}\big||x_1| - |x_2|\big| \le (|\tfrac{1}{\epsilon} - 1| + \tfrac{1}{\epsilon})|x_1 - x_2| \quad \forall x_1, x_2 \in \mathcal{K}_2. \end{aligned} \tag{2.12}$$

One can further derive

$$\begin{aligned} &|\nabla_x g_\epsilon(x_1;b) - \nabla_x g_\epsilon(x_2;b)| = |(1-\tfrac{1}{\epsilon})x_1 - (1-\tfrac{\sqrt{b}}{|x_2|})x_2| \\ \le &|1-\tfrac{1}{\epsilon}|\ |x_1-x_2| + |x_2||\tfrac{1}{\epsilon} - \tfrac{\sqrt{b}}{|x_2|}| \le (|\tfrac{1}{\epsilon} - 1| + \tfrac{1}{\epsilon})|x_1 - x_2| \quad \forall x_1 \in \mathcal{K}_1, x_2 \in \mathcal{K}_2. \end{aligned} \tag{2.13}$$

By (2.11)-(2.13), one gets

$$|\nabla_x g_\epsilon(x_1;b) - \nabla_x g_\epsilon(x_2;b)| \le (|\tfrac{1}{\epsilon} - 1| + \tfrac{1}{\epsilon})|x_1 - x_2| \quad \forall\ x_1, x_2 \in \mathbb{C}, \tag{2.14}$$

that demonstrates the Lipschitz continuity of $\nabla_x g_\epsilon(\cdot;b)$.

Finally one can derive

$$\begin{aligned} &\|\nabla_z \mathcal{G}_\epsilon(z;f) - \nabla_z \mathcal{G}_\epsilon(y;f)\| = \sqrt{\textstyle\sum_j \|\nabla_x g_\epsilon(z(j);f(j)) - \nabla_x g_\epsilon(y(j);f(j))\|^2} \\ \le &(|\tfrac{1}{\epsilon} - 1| + \tfrac{1}{\epsilon})\|z-y\| \quad \forall\ z,y \in \mathbb{C}^m, \end{aligned}$$

where the last relation is based on (2.14). That concludes this lemma. ∎

We remark that when considering the following optimization problem w.r.t. the solution on the entire region

$$\min_u \mathcal{G}_\epsilon(Au; f),$$

one can readily get the first-order optimality condition by (2.10)

$$A^*\big((\mathbf{1} - \tfrac{\sqrt{f}}{\max\{\epsilon\sqrt{f}, |Au|\}}) \circ Au\big) = 0,$$

where we assume that $f > 0$ as [30] (one can always remove the zero intensity values). It does not have singularity at the origin, and is exactly the first-order optimality condition for the AGM based optimization problem in the case of $\epsilon = 0$. Moreover, one can notice that the stationary points of the ST-AGM defined in (2.7) keep unchanged compared with those of AGM, and new metric only differs from the AGM near the origin (local maximum) by setting the truncation parameter $\epsilon \in (0, 1)$ in (2.7). Therefore, it should not affect the performance of new algorithm developed in the paper.

Hereafter, we consider the nonlinear optimization problem with ST-AGM. In order to enable the parallel computing of u_1 and u_2, we introduce an auxiliary variable v which is only defined in the overlapping region $\Omega_{1,2}$, and then are concerned with the following model:

$$\min_{u_1,u_2,v} \sum_{d=1}^{2} \mathcal{G}_\epsilon(A_d u_d; f_d) \qquad \text{s.t. } \pi_{d,3-d} u_d - v = 0,\ d = 1, 2. \tag{2.15}$$

2.3. Overlapping DD based ptychography algorithm (OD^{2}P). As one of the most popular first-order operator-splitting algorithm, the ADMM [15, 37, 2] has been applied to ptychography reconstruction, showing competitive performances for Poisson noisy measurements as well as large scan stepsizes [36, 5, 12]. We will also solve the proposed model (2.15) using ADMM.

In order to develop an iterative scheme without inner loop as well as with fast convergence for large-step scan, two auxiliary variables z_1, z_2 are introduced below:

$$\begin{aligned} &\min_{u_1,u_2,v,z_1,z_2} \sum_{d=1}^{2} \mathcal{G}_\epsilon(z_d; f_d) \\ &s.t.\ \ \pi_{d,3-d} u_d - v = 0, \quad A_d u_d - z_d = 0,\ d = 1, 2, \end{aligned} \tag{2.16}$$

and then introduce the corresponding augmented Lagrangian for (2.16) as follows:

$$\begin{aligned} \mathcal{L}(u_1, u_2, v, z_1, z_2, \Lambda_{1,2}, \Lambda_{2,1}, \Gamma_1, \Gamma_2) &:= \sum_{d=1}^{2} \mathcal{G}_\epsilon(z_d; f_d) \\ &+ r \sum_{d=1}^{2} \left(\Re(\langle \Lambda_{d,3-d}, \pi_{d,3-d} u_d - v \rangle) + \tfrac{1}{2} \|\pi_{d,3-d} u_d - v\|^2 \right) \\ &+ \eta \sum_{d=1}^{2} \left(\Re(\langle \Gamma_d, \mathcal{A}_d u_d - z_d \rangle) + \tfrac{1}{2} \|A_d u_d - z_d\|^2 \right), \end{aligned} \tag{2.17}$$

with $\Re(\cdot)$ denoting the real part of a complex number. Then we are concerned with the following saddle point problem below:

$$\max_{\Lambda_{1,2},\Lambda_{2,1},\Gamma_1,\Gamma_2} \quad \min_{u_1,u_2,v,z_1,z_2} \mathcal{L}(u_1, u_2, v, z_1, z_2, \Lambda_{1,2}, \Lambda_{2,1}, \Gamma_1, \Gamma_2). \tag{2.18}$$

To solve the saddle point problem (2.18), an iterative scheme using the alternating minimization is given below: To get $(u_1^{n+1}, u_2^{n+1}, v^{n+1}, z_1^{n+1}, z_2^{n+1}, \Gamma_1^{n+1}, \Gamma_2^{n+1}, \Lambda_{1,2}^{n+1}, \Lambda_{2,1}^{n+1})$ by the following steps:

(2.19)

$$\begin{cases} \text{Step 1.} \ (v^{n+1}, z_1^{n+1}, z_2^{n+1}) = \arg\min_{v,z_1,z_2} \mathcal{L}(u_1^n, u_2^n, v, z_1, z_2, \Lambda_{1,2}^n, \Lambda_{2,1}^n, \Gamma_1^n, \Gamma_2^n) \\ \qquad\qquad = \arg\min_{v,z_1,z_2} \sum_{d=1}^{2} \mathcal{G}_\epsilon(z_d; f_d) + \frac{\eta}{2} \sum_{d=1}^{2} \|z_d - (\Gamma_d^n + A_d u_d^n)\|^2 \\ \qquad\qquad\qquad + \frac{r}{2} \sum_{d=1}^{2} \left(\|v - (\pi_{d,3-d} u_d^n + \Lambda_{d,3-d}^n)\|^2 \right); \\ \text{Step 2.} \ \Gamma_d^{n+1} = \Gamma_d^n + A_d u_d^n - z_d^{n+1}, d = 1, 2; \\ \text{Step 3.} \ (u_1^{n+1}, u_2^{n+1}) = \arg\min_{u_1,u_2} \mathcal{L}(u_1, u_2, v^{n+1}, z_1^{n+1}, z_2^{n+1}, \Lambda_{1,2}^n, \Lambda_{2,1}^n, \Gamma_1^{n+1}, \Gamma_2^{n+1}) \\ \qquad\qquad = \arg\min_{u_1,u_2} \frac{\eta}{2} \sum_{d=1}^{2} \|A_d u_d + \Gamma_d^{n+1} - z_d^{n+1}\|^2 + \frac{r}{2} \sum_{d=1}^{2} \|\pi_{d,3-d} u_d - v^{n+1} + \Lambda_{d,3-d}^n\|^2; \\ \text{Step 4.} \ \Lambda_{d,3-d}^{n+1} = \Lambda_{d,3-d}^n + \pi_{d,3-d} u_d^{n+1} - v^{n+1}, d = 1, 2; \end{cases}$$

with the approximation solutions $(u_1^n, u_2^n, v^n, z_1^n, z_2^n, \Gamma_1^n, \Gamma_2^n, \Lambda_{1,2}^n, \Lambda_{2,1}^n)$ in the n^{th} step.

One readily knows that the objective functions for all subproblems (sub-optimization problem) of proposed ADMMs are differentiable, such that we have

$$\begin{cases} 0 = \nabla_{z_d} \mathcal{G}_\epsilon(z_d^{n+1}; f_d) - \eta \Gamma_d^{n+1}, \quad d = 1, 2; \\ 0 = v^{n+1} - \frac{1}{2} \sum_{d=1}^{2} (\pi_{d,3-d} u_d^n + \Lambda_{d,3-d}^n); \\ 0 = (r \pi_{d,3-d}^T \pi_{d,3-d} + \eta A_d^* A_d) u_d^{n+1} - \big(r \pi_{d,3-d}^T (v^{n+1} - \Lambda_{d,3-d}^n) + \eta A_d^* (z_d^{n+1} - \Gamma_d^{n+1})\big), d = 1, 2; \end{cases} \tag{2.20}$$

where the third equation is derived by taking partial gradient of the augmented Lagrangian and the multiplier update in (2.19). By (2.8) and the first two equations in (2.20), one can get closed forms of z_d^{n+1} and v^{n+1}. In order to get the solution for $u_d^{n+1}, d = 1, 2$, we further discuss how to solve the linear systems in the last two equations in (2.20). With the definition of A_d in (2.3), one can get

$$A_d^* A_d = \mathrm{diag}\big(\sum_{j_d=0}^{J_d - 1} (\mathcal{S}_{j_d}^d)^T |w|^2 \big), \ d = 1, 2. \tag{2.21}$$

One can also get $\pi_{d,3-d}^T \pi_{d,3-d} = R_d R_{d,3-d}^T R_{d,3-d} R_d^T = \mathrm{diag}(\boldsymbol{\sigma}_d), \ d = 1, 2$, with $\boldsymbol{\sigma}_d \in \mathbb{R}^{n_d}$ denoted as

$$\boldsymbol{\sigma}_d(j) = \begin{cases} 1, & \text{if } \ l_j^d \in \Omega_{1,2}; \\ 0, & \text{otherwise}, \end{cases} \quad \forall \ 0 \le j \le n_d - 1. \tag{2.22}$$

Therefore, $u_d^{n+1} (d = 1, 2)$ can be determined explicitly as below: $\forall \ 0 \le j_d \le n_d - 1$,

$$u_d^{n+1}(j_d) = \begin{cases} \frac{(r \pi_{d,3-d}^T (v^{n+1} - \Lambda_{d,3-d}^n) + \eta A_d^* (z_d^{n+1} - \Gamma_d^{n+1}))(j_d)}{r + \eta \sum_{j_d=0}^{J_d - 1} ((\mathcal{S}_{j_d}^d)^T |w|^2)(j_d)}, & \text{if } l_{j_d}^d \in \Omega_{1,2}; \\ \frac{(A_d^* (z_d^{n+1} - \Gamma_d^{n+1}))(j_d)}{\sum_{j_d=0}^{J_d - 1} ((\mathcal{S}_{j_d}^d)^T |w|^2)(j_d)}, & \text{otherwise.} \end{cases} \tag{2.23}$$

The overall overlapping DD based ptychography algorithm (OD^{2}P) is given as below:

Algorithm 1: **O**verlapping **DD** based **P**tychography algorithm (OD^{2}P)

Step 0. Initialize $u_1^0 = \mathbf{1}, u_2^0 = \mathbf{1}, v^0, \ z_1^0 = A_1 u_1^0, z_2^0 = A_2 u_2^0$, and multipliers $\Gamma_1^0 = \mathbf{0}, \Gamma_2^0 = \mathbf{0}, \Lambda_{1,2}^0 = \Lambda_{2,1}^0 = \mathbf{0}$. Set $n := 0$.

Step 1. Update z_1^{n+1} and z_2^{n+1} in parallel by

$$z_d^{n+1} = \mathrm{Prox}_{\mathcal{G}_\epsilon; \eta}(\Gamma_d^n + A_d u_d^n), d = 1, 2; \tag{2.24}$$

and update v^{n+1} by

$$v^{n+1} = \frac{1}{2} \sum_{d=1}^{2} (\pi_{d,3-d} u_d^n + \Lambda_{d,3-d}^n); \tag{2.25}$$

Step 2. Update multipliers $\Gamma_1^{n+1}, \Gamma_2^{n+1}$ in parallel by

$$\Gamma_d^{n+1} = \Gamma_d^n + A_d u_d^n - z_d^{n+1}, \quad d = 1, 2; \tag{2.26}$$

Step 3. Update u_1^{n+1}, u_2^{n+1} in parallel by (2.23).

Step 4. Update multipliers $\Lambda_{1,2}^{n+1}, \Lambda_{2,1}^{n+1}$ by

$$\Lambda_{d,3-d}^{n+1} = \Lambda_{d,3-d}^n + \pi_{d,3-d} u_d^{n+1} - v^{n+1}, \quad d = 1, 2. \tag{2.27}$$

Step 5. If satisfying the stopping condition, then stop and output u_1^{n+1} and u_2^{n+1} as the final solution; otherwise set $n := n + 1$, and go to Step 1.

2.4. Convergence analysis. First by the last equation in (2.20) and the multipliers update in (2.19), one can derive

$$0 = \eta A_d^*(A_d u_d^{n+1} + \Gamma_d^{n+1} - z_d^{n+1}) + r\pi_{d,3-d}^T \Lambda_{d,3-d}^{n+1}, d = 1, 2. \tag{2.28}$$

Assumption 1. *The matrices $A_d^* A_d$ $(d = 1, 2)$ are non-singular, i.e. there exists strictly positive constant $\hat{c}_d (d = 1, 2)$, s.t. $\|A_d h_d\| \geq \hat{c}_d \|h_d\| \quad \forall h_d \in \mathbb{C}^{n_d}$.*

The assumption is to guarantee the boundedness of the iterative sequence $\{u_d^n\}$, if $\{A_d u_d^n\}$ is bounded. By (2.21), the assumption holds with sufficiently small scan stepsize, i.e. each scan position and its neighbours have sufficient overlapping (one can also refer to Remark 4.1 of [5]).

Due to (2.9), one can prove that the function $\mathcal{G}_\epsilon(\cdot; f)$ has the descent property [5]:

$$\mathcal{G}_\epsilon(z; f) - \mathcal{G}_\epsilon(\hat{z}; f) - \Re(\langle \nabla_z \mathcal{G}_\epsilon(\hat{z}; f), z - \hat{z}\rangle) \leq \tfrac{L}{2}\|z - \hat{z}\|^2 \quad \forall\, z, \hat{z} \in \mathbb{C}^m. \tag{2.29}$$

Lemma 2.2. *Denote $E(z) = \frac{1}{2}\|Tz - f\|^2 + M(z)$, with convex function M and linear mapping T. Letting z^* be the global minimizer, i.e. $E(z^*) = \arg\min_z E(z)$, then we have*

$$E(z) - E(z^*) \geq \tfrac{1}{2}\|T(z - z^*)\|^2.$$

The proof of above lemma is trivial, and therefore we omit the details. Denote $X^n := (u_1^n, u_2^n, v^n, z_1^n, z_2^n, \Lambda_{1,2}^n, \Lambda_{2,1}^n, \Gamma_1^n, \Gamma_2^n)$. Then we can estimate the lower bound of the changes for the objective function values in the following lemma, that can further show the non-increasing of the sequence $\{\mathcal{L}(X^n)\}$ with proper parameters r and η (see Lemma 2.5).

Lemma 2.3.

$$\begin{aligned}
&\mathcal{L}(X^n) - \mathcal{L}(X^{n+1}) \\
&\geq \left(\tfrac{r}{2} - \tfrac{2\eta^2}{r}\|A_1^* A_1\|^2\right) \|\pi_{1,2}(u_1^n - u_1^{n+1})\|^2 + \left(\tfrac{r}{2} - \tfrac{2\eta^2}{r}\|A_2^* A_2\|^2\right) \|\pi_{2,1}(u_2^n - u_2^{n+1})\|^2 \\
&\quad + \left(\tfrac{\eta - 3L}{2} - \tfrac{L^2}{\eta} - \tfrac{2(L+\eta)^2}{r^2}\|\pi_{1,2} A_1^*\|^2\right) \|z_1^n - z_1^{n+1}\|^2 + \left(\tfrac{\eta - 3L}{2} - \tfrac{L^2}{\eta} - \tfrac{2(L+\eta)^2}{r^2}\|\pi_{2,1} A_2^*\|^2\right) \|z_2^n - z_2^{n+1}\|^2 \\
&\quad + r\|v^n - v^{n+1}\|^2 + \tfrac{\eta}{2}\sum_{d=1}^2 \|A_d(u_d^n - u_d^{n+1})\|^2
\end{aligned}$$

Proof. In order to estimate the decay of the augmented Lagrangian, the following relation [5] is given below:

$$\|z\|^2 - \|y\|^2 = \|z - y\|^2 + 2\Re\langle y, z - y\rangle \quad \forall\, z, y \in \mathbb{C}^m. \tag{2.30}$$

First for the z_d-subproblems, by (2.30), one readily has

$$\begin{aligned}
&\mathcal{L}(X^n) - \mathcal{L}(u_1^n, u_2^n, v^n, z_1^{n+1}, z_2^{n+1}, \Lambda_{1,2}^n, \Lambda_{2,1}^n, \Gamma_1^n, \Gamma_2^n) \\
&= \sum\nolimits_d \mathcal{G}_\epsilon(z_d^n; f_d) + \tfrac{\eta}{2}\|z_d^n - (\Gamma_d^n + A_d u_d^n)\|^2 - \left(\mathcal{G}_\epsilon(z_d^{n+1}; f_d) + \tfrac{\eta}{2}\|z_d^{n+1} - (\Gamma_d^n + A_d u_d^n)\|^2\right) \\
&\overset{(2.30)}{=} \sum\nolimits_d \left(\mathcal{G}_\epsilon(z_d^n; f_d) - \mathcal{G}_\epsilon(z_d^{n+1}; f_d) + \tfrac{\eta}{2}\|z_d^n - z_d^{n+1}\|^2 + \eta\Re(\langle z_d^{n+1} - (\Gamma_d^n + A_d u_d^n), z_d^n - z_d^{n+1}\rangle)\right) \\
&\overset{(2.19)}{=} \sum\nolimits_d \left(\mathcal{G}_\epsilon(z_d^n; f_d) - \mathcal{G}_\epsilon(z_d^{n+1}; f_d) + \tfrac{\eta}{2}\|z_d^n - z_d^{n+1}\|^2 - \eta\Re(\langle \Gamma_d^{n+1}, z_d^n - z_d^{n+1}\rangle)\right) \\
&\overset{(2.29)}{\geq} \sum\nolimits_d \left(\Re(\langle \nabla_z \mathcal{G}_\epsilon(z_d^n; f_d) - \eta\Gamma_d^{n+1}, z_d^n - z_d^{n+1}\rangle) + \tfrac{\eta - L}{2}\|z_d^n - z_d^{n+1}\|^2\right).
\end{aligned}$$

Further by the first equation in (2.20), (2.9) and Cauchy's inequality $\Re(\langle z, y\rangle) \geq -\frac{L}{2}\|z\|^2 - \frac{1}{2L}\|y\|^2$, one gets

$$\mathcal{L}(X^n) - \mathcal{L}(u_1^n, u_2^n, v^n, z_1^{n+1}, z_2^{n+1}, \Lambda_{1,2}^n, \Lambda_{2,1}^n, \Gamma_1^n, \Gamma_2^n) \geq \tfrac{\eta - 3L}{2}\sum\nolimits_d \|z_d^n - z_d^{n+1}\|^2. \tag{2.31}$$

For $v-$subproblem, it is quite standard, and we omit the details. Hence combined with (2.31), one gets

$$\mathcal{L}(X^n) - \mathcal{L}(u_1^n, u_2^n, v^{n+1}, z_1^{n+1}, z_2^{n+1}, \Lambda_{1,2}^n, \Lambda_{2,1}^n, \Gamma_1^n, \Gamma_2^n) \geq \tfrac{\eta - 3L}{2}\sum\nolimits_d \|z_d^n - z_d^{n+1}\|^2 + r\|v^n - v^{n+1}\|^2. \tag{2.32}$$

For the multipliers update $\{\Gamma_d^n\}$, one gets

$$\begin{aligned}&\mathcal{L}(u_1^n,u_2^n,v^{n+1},z_1^{n+1},z_2^{n+1},\Lambda_{1,2}^n,\Lambda_{2,1}^n,\Gamma_1^n,\Gamma_2^n)-\mathcal{L}(u_1^n,u_2^n,v^{n+1},z_1^{n+1},z_2^{n+1},\Lambda_{1,2}^n,\Lambda_{2,1}^n,\Gamma_1^{n+1},\Gamma_2^{n+1})\\ =&-\eta\sum\nolimits_d\|\Gamma_d^n-\Gamma_d^{n+1}\|^2\geq-\tfrac{L^2}{\eta}\sum\nolimits_d\|z_d^n-z_d^{n+1}\|^2,\end{aligned}\tag{2.33}$$

where the last equation is derived by the first equation in (2.20) and (2.9).

For the sequences $\{u_d^n\}$, based on Lemma 2.2, one gets

$$\begin{aligned}&\mathcal{L}(u_1^n,u_2^n,v^{n+1},z_1^{n+1},z_2^{n+1},\Lambda_{1,2}^n,\Lambda_{2,1}^n,\Gamma_1^{n+1},\Gamma_2^{n+1})-\mathcal{L}(u_1^{n+1},u_2^{n+1},v^{n+1},z_1^{n+1},z_2^{n+1},\Lambda_{1,2}^n,\Lambda_{2,1}^n,\Gamma_1^{n+1},\Gamma_2^{n+1})\\ \geq&\tfrac{\eta}{2}\sum\nolimits_d\|A_d(u_d^n-u_d^{n+1})\|^2+\tfrac{r}{2}\left(\|\pi_{1,2}(u_1^n-u_1^{n+1})\|^2+\|\pi_{2,1}(u_2^n-u_2^{n+1})\|^2\right).\end{aligned}\tag{2.34}$$

For the multipliers $\{\Lambda_{1,2}^n\}$ and $\{\Lambda_{2,1}^n\}$ update, by (2.28), one has $\Lambda_{1,2}^{n+1}=\frac{\eta}{r}\pi_{1,2}A_1^*(A_1u_1^{n+1}+\Gamma_1^{n+1}-z_1^{n+1})$ $=\frac{\eta}{r}\pi_{1,2}A_1^*A_1\pi_{1,2}^T(\pi_{1,2}u_1^{n+1})+\frac{1}{r}\pi_{1,2}A_1^*\nabla_{z_1}\mathcal{G}_\epsilon(z_1^{n+1};f_1)-\frac{\eta}{r}\pi_{1,2}A_1^*z_1^{n+1}$, by the first equation in (2.20) and $A_1^*A_1$ being diagonal matrix. Then by (2.9), one can estimate the successive error of the multiplier $\{\Lambda_{1,2}^n\}$ as $\|\Lambda_{1,2}^n-\Lambda_{1,2}^{n+1}\|\leq\frac{\eta}{r}\|A_1^*A_1\|\ \|\pi_{1,2}(u_1^n-u_1^{n+1})\|+\frac{L+\eta}{r}\ \|\pi_{1,2}A_1^*\|\ \|z_1^n-z_1^{n+1}\|$. By the inequality $(a+b)^2\leq 2(a^2+b^2)\ \forall\ a,b\in\mathbb{R}$, one immediately obtains

$$\|\Lambda_{1,2}^n-\Lambda_{1,2}^{n+1}\|^2\leq\tfrac{2\eta^2}{r^2}\|A_1^*A_1\|^2\ \|\pi_{1,2}(u_1^n-u_1^{n+1})\|^2+\tfrac{2(L+\eta)^2}{r^2}\ \|\pi_{1,2}A_1^*\|^2\ \|z_1^n-z_1^{n+1}\|^2,\tag{2.35}$$

Similarly, one can get

$$\|\Lambda_{2,1}^n-\Lambda_{2,1}^{n+1}\|^2\leq\tfrac{2\eta^2}{r^2}\|A_2^*A_2\|^2\ \|\pi_{2,1}(u_2^n-u_2^{n+1})\|^2+\tfrac{2(L+\eta)^2}{r^2}\ \|\pi_{2,1}A_2^*\|^2\ \|z_2^n-z_2^{n+1}\|^2.\tag{2.36}$$

Combined with (2.35) and (2.36), one gets

$$\begin{aligned}&\mathcal{L}(u_1^{n+1},u_2^{n+1},v^{n+1},z_1^{n+1},z_2^{n+1},\Lambda_{1,2}^n,\Lambda_{2,1}^n,\Gamma_1^{n+1},\Gamma_2^{n+1})-\mathcal{L}(X^{n+1})\\ =&-r\|\Lambda_{1,2}^n-\Lambda_{1,2}^{n+1}\|^2-r\|\Lambda_{2,1}^n-\Lambda_{2,1}^{n+1}\|^2\\ \geq&-\tfrac{2\eta^2}{r}\|A_1^*A_1\|^2\ \|\pi_{1,2}(u_1^n-u_1^{n+1})\|^2-\tfrac{2\eta^2}{r}\|A_2^*A_2\|^2\ \|\pi_{2,1}(u_2^n-u_2^{n+1})\|^2\\ &-\tfrac{2(L+\eta)^2}{r^2}\ \|\pi_{1,2}A_1^*\|^2\ \|z_1^n-z_1^{n+1}\|^2-\tfrac{2(L+\eta)^2}{r^2}\ \|\pi_{2,1}A_2^*\|^2\ \|z_2^n-z_2^{n+1}\|^2.\end{aligned}\tag{2.37}$$

Summing up (2.32), (2.33), (2.34), and (2.37) concludes this lemma. □

Lemma 2.4. *The augmented Lagrangian is lower bounded, i.e.* $\mathcal{L}(X^n)>-\infty$, *if*

$$(r,\eta)\in\left\{(r,\eta)\in\mathbb{R}_+^2:\ \eta-1\geq 0, r-\eta\max\{\|\pi_{1,2}A_1^*\|,\|\pi_{2,1}A_2^*\|\}\geq 0\right\}.$$

Proof. First we have

$$\begin{aligned}\mathcal{L}(X^{n+1}):=&\sum\nolimits_d\mathcal{G}_\epsilon(z_d^{n+1};f_d)\\ &+\tfrac{r}{2}\|\pi_{1,2}u_1^{n+1}-v^{n+1}+\Lambda_{1,2}^{n+1}\|^2-\tfrac{r}{2}\|\Lambda_{1,2}^{n+1}\|^2\\ &+\tfrac{r}{2}\|\pi_{2,1}u_2^{n+1}-v^{n+1}+\Lambda_{2,1}^{n+1}\|^2-\tfrac{r}{2}\|\Lambda_{2,1}^{n+1}\|^2\\ &+\eta\sum\nolimits_d\left(\tfrac{1}{2}\|A_du_d^{n+1}-z_d^{n+1}+\Gamma_d^{n+1}\|^2-\tfrac{1}{2}\|\Gamma_d^{n+1}\|^2\right)\\ \overset{(2.20),(2.28)}{=}&\ \tfrac{r}{2}\|\pi_{1,2}u_1^{n+1}-v^{n+1}+\Lambda_{1,2}^{n+1}\|^2-\tfrac{\eta^2}{2r}\|\pi_{1,2}A_1^*(A_1u_1^{n+1}+\Gamma_1^{n+1}-z_1^{n+1})\|^2\\ &+\tfrac{r}{2}\|\pi_{2,1}u_2^{n+1}-v^{n+1}+\Lambda_{2,1}^{n+1}\|^2-\tfrac{\eta^2}{2r}\|\pi_{2,1}A_2^*(A_2u_2^{n+1}+\Gamma_2^{n+1}-z_2^{n+1})\|^2\\ &+\sum\nolimits_d\left(\tfrac{\eta}{2}\|A_du_d^{n+1}-z_d^{n+1}+\Gamma_d^{n+1}\|^2+\mathcal{G}_\epsilon(z_d^{n+1};f_d)-\tfrac{1}{2\eta}\|\nabla_{z_d}\mathcal{G}_\epsilon(z_d^{n+1};f_d)\|^2\right)\\ \geq&\ \tfrac{r}{2}\|\pi_{1,2}u_1^{n+1}-v^{n+1}+\Lambda_{1,2}^{n+1}\|^2+\tfrac{r}{2}\|\pi_{2,1}u_2^{n+1}-v^{n+1}+\Lambda_{2,1}^{n+1}\|^2\\ &+\sum\nolimits_d\left(\tfrac{\eta}{2}(1-\tfrac{\eta}{r}\max\{\|\pi_{1,2}A_1^*\|,\|\pi_{2,1}A_2^*\|\})\ \|A_du_d^{n+1}-z_d^{n+1}+\Gamma_d^{n+1}\|^2\right)\\ &+\sum\nolimits_{d,j}\left(g_\epsilon(z_d^{n+1}(j),f_d(j))-\tfrac{1}{2\eta}\|\nabla_x g_\epsilon(z_d^{n+1}(j),f_d(j))\|^2\right).\end{aligned}$$

By the definition of (2.7) and its gradient (2.10), one gets

$$\begin{aligned}
&\sum\nolimits_{d,j}\Big(g_\epsilon(z_d^{n+1}(j),f_d(j))-\tfrac{1}{2\eta}\|\nabla_x g_\epsilon(z_d^{n+1}(j),f_d(j))\|^2\Big)\\
=&\sum\nolimits_d\tfrac{1}{2}(1-\tfrac{1}{\eta})\sum\nolimits_{j_1\in\{j:\ |z_d^{n+1}(j)|>=\epsilon\sqrt{f_d(j)}\}}\big||z_d^{n+1}(j_1)|-\sqrt{f_d(j_1)}\big|^2\\
&+\sum\nolimits_d\sum\nolimits_{j_2\in\{j:\ |z_d^{n+1}(j)|<\epsilon\sqrt{f_d(j)}\}}\Big(\tfrac{1-\epsilon}{2}f_d(j_2)-\tfrac{1-\epsilon}{2\epsilon}(1+\tfrac{1-\epsilon}{\eta\epsilon})|z_d^{n+1}(j_2)|^2\Big).
\end{aligned}$$

Hence one gets

$$\begin{aligned}
\mathcal{L}(X^{n+1})\geq&\tfrac{r}{2}\|\pi_{1,2}u_1^{n+1}-v^{n+1}+\Lambda_{1,2}^{n+1}\|^2+\tfrac{r}{2}\|\pi_{2,1}u_2^{n+1}-v^{n+1}+\Lambda_{2,1}^{n+1}\|^2\\
&+\sum\nolimits_d\big(\tfrac{\eta}{2}(1-\tfrac{\eta}{r}\max\{\|\pi_{1,2}A_1^*\|,\|\pi_{2,1}A_2^*\|\})\ \|A_du_d^{n+1}-z_d^{n+1}+\Gamma_d^{n+1}\|^2\big)\\
&+\sum\nolimits_d\tfrac{1}{2}(1-\tfrac{1}{\eta})\sum\nolimits_{j_1\in\{j:\ |z_d^{n+1}(j)|>=\epsilon\sqrt{f_d(j)}\}}\big||z_d^{n+1}(j_1)|-\sqrt{f_d(j_1)}\big|^2\\
&+\sum\nolimits_d\sum\nolimits_{j_2\in\{j:\ |z_d^{n+1}(j)|<\epsilon\sqrt{f_d(j)}\}}\Big(\tfrac{1-\epsilon}{2}f_d(j_2)-\tfrac{1-\epsilon}{2\epsilon}(1+\tfrac{1-\epsilon}{\eta\epsilon})|z_d^{n+1}(j_2)|^2\Big).
\end{aligned}\tag{2.38}$$

Readily one knows the last term is bounded since $|z_d^{n+1}(j_2)|<\epsilon\sqrt{f_d(j_2)}$. By setting $\eta\geq 1$ and $r\geq\eta\max\{\|\pi_{1,2}A_1^*\|,\|\pi_{2,1}A_2^*\|\}$, one can immediately conclude this lemma.
□

Lemma 2.5. *Letting $(r,\eta)\in\mathcal{K}$ with*

$$\begin{aligned}
\mathcal{K}:=\Big\{(r,\eta)\in\mathbb{R}_+^2:\ \ &\eta-1\geq 0,\quad r-\eta\max\{2\|A_1^*A_1\|,2\|A_2^*A_2\|,\|\pi_{1,2}A_1^*\|,\|\pi_{2,1}A_2^*\|\}>0,\\
&\tfrac{\eta-3L}{2}-\tfrac{L^2}{\eta}-\tfrac{2(L+\eta)^2}{r^2}\max\{\|\pi_{1,2}A_1^*\|^2,\|\pi_{2,1}A_2^*\|^2\}>0\Big\},
\end{aligned}\tag{2.39}$$

the following assertions hold:

(1) The sequence $\{\mathcal{L}(X^n)\}$ is non-increasing with the finite lower bound.

(2) The following successive error converges to zero, i.e.

$$\lim_{n\to+\infty}X^n-X^{n+1}=\mathbf{0},\tag{2.40}$$

(3) The iterative sequence $\{X^n\}$ is bounded under Assumption 1.

Before giving the detailed proof, we will show that the set $\mathcal{K}$ is nonempty. By denoting

$$c_0:=\max\{2\|A_1^*A_1\|,2\|A_2^*A_2\|,\|\pi_{1,2}A_1^*\|,\|\pi_{2,1}A_2^*\|\},\qquad c_1:=2\max\{\|\pi_{1,2}A_1^*\|^2,\|\pi_{2,1}A_2^*\|^2\},$$

and letting $\eta\geq 1, r>c_0\eta$, we further have $c_1\frac{(L+\eta)^2}{r^2}<\frac{c_1}{c_0^2}\frac{(L+\eta)^2}{\eta^2}=\frac{c_1}{c_0^2}(L/\eta+1)^2\leq\frac{c_1}{c_0^2}(L+1)^2$ (the first inequality is based on $r>c_0\eta$, and the second is based on $\eta\geq 1$). Therefore, one just needs to guarantee the following inequality $\frac{\eta-3L}{2}-\frac{L^2}{\eta}-\frac{c_1}{c_0^2}(L+1)^2>0$, with choosing proper η. By letting $\eta>6L+2L^2+\frac{2c_1}{c_0^2}(L+1)^2$, the above inequality holds. Finally setting (r,η) in the nonempty set $\big\{(r,\eta):\ \ \frac{r}{c_0}>\eta>\max\{6L+2L^2+\frac{2c_1}{c_0^2}(L+1)^2,1\}\big\}$, it also belongs to the set $\mathcal{K}$, that immediately implies it is nonempty. Roughly to say, with big enough parameters η and r (r is no less than η with a constant factor), the above lemma holds.

Proof. The first two items (Items (1)-(2)) can be easily proved by Lemmas 2.3-2.4, (2.20), and (2.28). Notice that the last inequality of (2.39) is required in order to guarantee the positivity of the coefficients for the terms related with $\|z_d^n-z_d^{n+1}\|, d=1,2$.

One can readily get the boundedness of $\{z_d^n\}$ by (2.38). By the first equation of (2.20) and continuity of $\nabla_{z_d}\mathcal{G}_\epsilon(z_d;f_d)$, the sequences $\{\Gamma_d^n\}$ are also bounded. Since $\{A_du_d^n-z_d^n+\Gamma_d^n\}$ are bounded by (2.38) and Assumption 1, one can further conclude the boundedness of $\{u_d^n\}$. By (2.28), one can get the boundedness of $\{\Lambda_{1,2}^n\}$ and $\{\Lambda_{2,1}^n\}$, as well as the boundedness of $\{v^n\}$. That finishes the proof of Item (3). □

Theorem 1 (subsequence convergence). *Letting $(r,\eta)\in\mathcal{K}$, any limit point of $\{X^n\}$ is the stationary point of the saddle point problem (2.18) under Assumption 1.*

Proof. By Lemma 2.5 and (2.20)-(2.28), one can readily prove that any limit point $X^\star := (u_1^\star, u_2^\star, v^\star, z_1^\star, z_2^\star, \Lambda_{1,2}^\star, \Lambda_{2,1}^\star, \Gamma_1^\star, \Gamma_2^\star)$ of the iterative sequence satisfies the following equations

$$
\begin{aligned}
&0 = \nabla_{z_d}\mathcal{G}_\epsilon(z_d^\star; f_d) - \eta\Gamma_d^\star;\\
&0 = v^\star - \tfrac{1}{2}\sum\nolimits_{d=1}^{2}(\pi_{d,3-d}u_d^\star + \Lambda_{d,3-d}^\star);\\
&0 = (r\pi_{d,3-d}^T\pi_{d,3-d} + \eta A_d^*A_d)u_d^\star - \big(r\pi_{d,3-d}^T(v^\star - \Lambda_{d,3-d}^\star) + \eta A_d^*(z_d^\star - \Gamma_d^\star)\big), d = 1,2;\\
&0 = A_du_d^\star - z_d^\star;\\
&0 = \pi_{d,3-d}u_d^\star - v^\star, d = 1,2;
\end{aligned}
\tag{2.41}
$$

By the last two equations of the above relation, it can be simplified below:

$$
\begin{aligned}
&0 = \nabla_{z_d}\mathcal{G}_\epsilon(z_d^\star; f_d) - \eta\Gamma_d^\star,\ d = 1,2;\\
&0 = \Lambda_{1,2}^\star + \Lambda_{2,1}^\star;\\
&0 = r\pi_{d,3-d}^T\Lambda_{d,3-d}^\star + \eta A_d^*\Gamma_d^\star, d = 1,2;\\
&0 = A_du_d^\star - z_d^\star,\ d = 1,2;\\
&0 = \pi_{d,3-d}u_d^\star - v^\star, d = 1,2,
\end{aligned}
\tag{2.42}
$$

that is exactly the stationary point of (2.18), and therefore it finishes the proof. ∎

Theorem 2 (global convergence). *Letting $(r,\eta) \in \mathcal{K}$, the iterative sequence $\{X^n\}$ converges to the stationary point of the saddle point problem (2.18) under Assumption 1.*

Proof. It is quite standard to prove that the gradient of the augmented Lagrangian is bounded by the $\|X^n - X^{n+1}\|$, which simply follows Lemma 4.3 of [5]. One just needs to show that the augmented Lagrangian with the ST-AGM metric is semi-algebraic function. First, the graph of the $g_\epsilon(z_d(j), f_d(j))$ is semi-algebraic (We study this property by separating the real and imaginary parts of the complex-valued variables following [5]), since it can be expressed by

$$
\begin{aligned}
&\Big(\{(z_{d,r}(j), z_{d,i}(j), F(j)) \in \mathbb{R}^3 :\ F(j) - \tfrac{1-\epsilon}{2}(f_d(j) - \tfrac{1}{\epsilon}((z_{d,r}(j))^2 + (z_{d,i}(j))^2)) = 0\}\\
&\quad \cap \{(z_{d,r}(j), z_{d,i}(j), F(j)) \in \mathbb{R}^3 :\ (z_{d,r}(j))^2 + (z_{d,i}(j))^2 - \epsilon^2 f_d(j) < 0\}\Big)\\
&\bigcup\Big(\{(z_{d,r}(j), z_{d,i}(j), F(j)) \in \mathbb{R}^3 :\ \tfrac{1}{2}((z_{d,r}(j))^2 + (z_{d,i}(j))^2 + f_d(j)) - F(j) \geq 0\}\\
&\cap \{(z_{d,r}(j), z_{d,i}(j), F(j)) \in \mathbb{R}^3 : (\tfrac{1}{2}((z_{d,r}(j))^2 + (z_{d,i}(j))^2 + f_d(j)) - F(j))^2 - f_d(j)((z_{d,r}(j))^2 + (z_{d,i}(j))^2) = 0\}\\
&\quad \cap \{(z_{d,r}(j), z_{d,i}(j), F(j)) \in \mathbb{R}^3 :\ (z_{d,r}(j))^2 + (z_{d,i}(j))^2 - \epsilon^2 f_d(j) \geq 0\}\Big),
\end{aligned}
$$

with $z_d(j) := z_{d,r}(j) + \boldsymbol{i}z_{d,i}(j)$ and $\boldsymbol{i}^2 = -1$. Immediately one sees that the function $D_j(z_d; f_d) := g_\epsilon(z_d(j); f_d(j))$ is semi-algebraic. Then ST-AGM $\mathcal{G}_\epsilon(z_d; f_d) = \sum_j D_j(z_d; f_d)$ is also semi-algebraic since the finite sum of the algebraic functions are also semi-algebraic [1]. Since other terms other than ST-AGM are also semi-algebraic, the augmented Lagrangian function $\mathcal{L}(X)$ is semi-algebraic. Thus one concludes this theorem based on Theorem 1, the gradient of augmented Lagrangian bounded by $\|X^n - X^{n+1}\|$ and semi-algebraic property following [1]. ∎

We remark that Theorem 1 demonstrates that limit point of iterative sequence satisfies the constraint $\pi_{1,2}u_1 = \pi_{2,1}u_2$. Denote

$$
\forall 0 \leq j \leq n-1, \quad u^\star(j) := \begin{cases} (R_1^T u_1^\star)(j), & \text{if } j \in \Omega_1 \setminus \Omega_{1,2};\\ (R_{1,2}^T v^\star)(j), & \text{if } j \in \Omega_{1,2};\\ (R_2^T u_2^\star)(j), & \text{otherwise;}\end{cases}
$$

$z^\star := Au^\star$, and $\Gamma^\star := (\Gamma_1^T, \Gamma_2^T)^T$. Further with the given stationary point system (2.42), we have

$$
\begin{cases} 0 = \nabla_z\mathcal{G}_\epsilon(z^\star; f) - \eta\Gamma^\star,\\ 0 = Au^\star - z^\star,\\ 0 = A^*\Gamma^\star,\end{cases}
$$

Then we get $A^*\nabla_z \mathcal{G}_\epsilon(Au^\star; f) = 0$, that is exactly the first-order optimality condition for the optimization problem on the whole domain as $\min_u \mathcal{G}_\epsilon(Au; f)$. Hence, by merging these two sub-solutions, Theorem 2 actually demonstrates the proposed algorithm is able to produce the stationary point for the original optimization problem defined on the whole domain.

3. Extensions. In this part, we mainly discuss further extensions for multiple-subdomain DD (more than two) and blind recovery.

3.1. Multiple-subdomain DD. We consider the DD with D subdomains ($D \geq 2$). Denote the overlapping DD as $\Omega := \bigcup_{d=1}^D \Omega_d$, and there exists a non-empty index set $\widetilde{\mathscr{N}} := \{(i_1, i_2) : \Omega_{i_1} \bigcap \Omega_{i_2} \neq \emptyset \; \forall 1 \leq i_1, i_2 \leq D\}$ denoting the index pairs for overlapped subdomains, and $\mathscr{N} := \{(i_1, i_2) \in \widetilde{\mathscr{N}} : \; i_1 < i_2\}$. In a similar manner to the two-subdomain case in the last section, one can denote $A_d, f_d (1 \leq d \leq D)$ and the restriction operator $\pi_{i_1,i_2} \; \forall (i_1, i_2) \in \mathscr{N}$ from the subdomain Ω_{i_1} to the overlapping region Ω_{i_1,i_2} between the subdomains Ω_{i_1} and Ω_{i_2}, such that to get the solution u_d on the subdomain $\Omega_d \forall 1 \leq d \leq D$, one has to solve the following equations:

$$|A_d u_d|^2 = f_d \; \forall 1 \leq d \leq D; \; \pi_{i_1,i_2} u_{i_1} = \pi_{i_2,i_1} u_{i_2} \; \forall (i_1, i_2) \in \mathscr{N}, \tag{3.1}$$

that exactly extends (2.4) and (2.5) to multiple subdomains DD. The following constraint optimization problem is given by introducing auxiliary variables $\{z_d\}_{d=1}^D$ and $\{v_{i_1,i_2}\}_{(i_1,i_2)\in\mathscr{N}}$

$$\begin{aligned} &\min_{\{u_d\}_{d=1}^D, \{v_{i_1,i_2}\}_{(i_1,i_2)\in\mathscr{N}}} \quad \sum_{d=1}^D \mathcal{G}_\epsilon(z_d; f_d) \\ &s.t. \; \pi_{i_1,i_2} u_{i_1} - v_{i_1,i_2} = 0, \pi_{i_2,i_1} u_{i_2} - v_{i_1,i_2} = 0 \quad (i_1, i_2) \in \mathscr{N}, \\ &\quad z_d - A_d u_d = 0, \; 1 \leq d \leq D. \end{aligned}$$

Similar to the two-subdomain case, the corresponding augmented Lagrangian is given below:

$$\begin{aligned} \mathcal{L}_m(\{u_d\}, \{v_{i_1,i_2}\}_{(i_1,i_2)\in\mathscr{N}}, \{z_d\}, \{\Lambda_{i_1,i_2}\}_{(i_1,i_2)\in\widetilde{\mathscr{N}}}, \{\Gamma_d\}) &:= \sum_{d=1}^D \mathcal{G}_\epsilon(z_d; f_d) \\ + \sum_{(i_1,i_2)\in\mathscr{N}} \left(r\Re(\langle \Lambda_{i_1,i_2}, \pi_{i_1,i_2} u_{i_1} - v_{i_1,i_2} \rangle) + \tfrac{r}{2} \|\pi_{i_1,i_2} u_{i_1} - v_{i_1,i_2}\|^2 \right) \\ + \sum_{(i_1,i_2)\in\mathscr{N}} \left(r\Re(\langle \Lambda_{i_2,i_1}, \pi_{i_2,i_1} u_{i_2} - v_{i_1,i_2} \rangle) + \tfrac{r}{2} \|\pi_{i_2,i_1} u_{i_2} - v_{i_1,i_2}\|^2 \right) \\ + \eta \sum_{d=1}^D \left(\Re(\langle \Gamma_d, \mathcal{A}_d u_d - z_d \rangle) + \tfrac{1}{2} \|A_d u_d - z_d\|^2 \right), \end{aligned} \tag{3.2}$$

with multipliers $\{\Lambda_{i_1,i_2}\}_{(i_1,i_2)\in\widetilde{\mathscr{N}}}$ and $\{\Gamma_d\}_{d=1}^D$.

We only analyze the u_d-subproblem which is different from the two-subdomain case in Algorithm 1. One has

$$\min_{u_d} \left(\sum_{(d,i_2)\in\mathscr{N}} \tfrac{r}{2} \|\Lambda_{d,i_2} + \pi_{d,i_2} u_d - v_{d,i_2}\|^2 + \sum_{(i_1,d)\in\mathscr{N}} \tfrac{r}{2} \|\Lambda_{d,i_1} + \pi_{d,i_1} u_d - v_{i_1,d}\|^2 \right) + \tfrac{\eta}{2} \|A_d u_d - z_d + \Gamma_d\|^2,$$

such that the first order optimality condition is given as

$$\begin{aligned} &\left(\eta A_d^* A_d + r \sum_{(d,i_2),(i_1,d)\in\mathscr{N}} (\pi_{d,i_1}^T \pi_{d,i_1} + \pi_{d,i_2}^T \pi_{d,i_2}) \right) u_d \\ =&\eta A_d^* (z_d - \Gamma_d) + r \sum_{(d,i_2)\in\mathscr{N}} \pi_{d,i_2}^T (v_{d,i_2} - \Lambda_{d,i_2}) + r \sum_{(i_1,d)\in\mathscr{N},} \pi_{d,i_1}^T (v_{i_1,d} - \Lambda_{d,i_1}). \end{aligned}$$

Similar to the case of two-subdomain, this subproblem has closed-form solution as (2.23), such that it can also be very efficiently solved.

Similar to the two subdomain decomposition, the overall overlapping DD based ptychography algorithm for multiple subdomains (OD^{2}P$_m$) is given as below:

Algorithm 2: **O**verlapping **DD** based **P**tychography algorithm for **M**ultiple Subdomains (OD^{2}P$_m$)

Step 0. Initialize $u_d^0 = \mathbf{1}, \{v_{i_1,i_2}^0\}$, $z_d^0 = A_d u_d^0$, and multipliers $\Gamma_d^0 = \mathbf{0}, \Lambda_{i_1,i_2}^0 = \mathbf{0}$. Set $n := 0$.

Step 1. Update $\{z_d^{n+1}\}_{d=1}^D$ by (2.24) and update $\{v_{i_1,i_2}^{n+1}\}_{(i_1,i_2)\in\mathscr{N}}$ by

$$v_{i_1,i_2}^{n+1} = \tfrac{1}{2}(\pi_{i_1,i_2} u_{i_1}^n + \pi_{i_2,i_1} u_{i_2}^n + \Lambda_{i_1,i_2}^n + \Lambda_{i_2,i_1}^n); \tag{3.3}$$

Step 2. Update multipliers in parallel by

$$\Gamma_d^{n+1} = \Gamma_d^n + A_d u_d^n - z_d^{n+1} \ \forall\ 1 \le d \le D; \tag{3.4}$$

Step 3. Update $\{u_d^{n+1}\}_{d=1}^D$ in parallel by

$$\begin{aligned} u_d^{n+1} = &\Big(\eta A_d^* A_d + r\sum\nolimits_{(d,i_2),(i_1,d)\in\mathscr{N}} (\pi_{d,i_1}^T \pi_{d,i_1} + \pi_{d,i_2}^T \pi_{d,i_2})\Big)^{-1} \\ \times &\Big(\eta A_d^*(z_d^{n+1} - \Gamma_d^{n+1}) + r\sum\nolimits_{(d,i_2)\in\mathscr{N}} \pi_{d,i_2}^T (v_{d,i_2}^{n+1} - \Lambda_{d,i_2}^n) + r\sum\nolimits_{(i_1,d)\in\mathscr{N},} \pi_{d,i_1}^T (v_{i_1,d}^{n+1} - \Lambda_{d,i_1}^n)\Big); \end{aligned}$$

Step 4. Update multipliers by

$$\begin{aligned} \Lambda_{i_1,i_2}^{n+1} &= \Lambda_{i_1,i_2}^n + \pi_{i_1,i_2} u_{i_1}^{n+1} - v_{i_1,i_2}^{n+1}, \\ \Lambda_{i_2,i_1}^{n+1} &= \Lambda_{i_2,i_1}^n + \pi_{i_2,i_1} u_{i_2}^{n+1} - v_{i_2,i_1}^{n+1}, \end{aligned} \tag{3.5}$$

for all $(i_1, i_2) \in \mathscr{N}$.

Step 5. If satisfying the stopping condition, then stop and output u_d^{n+1} as the final solution; otherwise set $n := n + 1$, and go to Step 1.

Among all the variables update in Algorithm 2, most variables (except v_{i_1,i_2}^{n+1} and the multipliers Λ_{i_1,i_2}^{n+1}) can be computed independently of other variables defined on another subdomain. The information of overlapping regions v_{i_1,i_2}^{n+1} is synchronized by the overlapping parts of two sub-solutions $u_{i_1}^n, u_{i_2}^n$, as well as the multiplier Λ_{i_1,i_2}. Hence, in principle the proposed OD^{2}P$_m$ can be implemented highly parallel, since the communications only happen at the boundary layers (much smaller sizes compared with the entire image).

For the convergence analysis, it is almost the same as the case of two subdomains and therefore we omit the details and give the convergence theorem directly as below:

Theorem 3. *Letting $(r, \eta) \in \mathcal{K}_D$ with*

$$\begin{aligned} \mathcal{K}_D := \Big\{(r,\eta) \in \mathbb{R}_+^2 :\ \ &\eta \ge 1, r - 2\eta \max\{\|A_d^* A_d\|^2\}_{d=1}^D > 0, \\ &\tfrac{\eta - 3L}{2} - \tfrac{L^2}{\eta} - \tfrac{2(L+\eta)^2}{r^2} \max_{(i_1,i_2)\in\mathscr{N}} \max\{\|\pi_{i_1,i_2} A_{i_1}^*\|^2, \|\pi_{i_2,i_1} A_{i_2}^*\|^2\} > 0\Big\}, \end{aligned} \tag{3.6}$$

then under Assumption 1 for $D-$subdomains, the iterative sequence $\widetilde{X}^n := \big(\{u_d^n\}, \{v_{i_1,i_2}^n\}_{(i_1,i_2)\in\mathscr{N}}, \{z_d^n\}, \{\Lambda_{i_1,i_2}^n\}_{(i_1,i_2)\in\widetilde{\mathscr{N}}}, \{\Gamma_d^n\}_{d=1}^D\big)$ generated by OD^2P_m converges to the stationary point of the saddle point problem of the augmented Lagrangian defined in (3.2).

Similar to the 2-subdomain case, the set (3.6) of the parameters r, η is nonempty.

3.2. Blind ptychography . To reduce the grid pathology [5] (ambiguity derived by the multiplication of any periodical function and the true solution) due to grid scan, introduce the support set constraint of the probe, i.e. $\mathcal{O} := \{w :\ (\mathcal{F}w)(j) = 0,\ j \in \bar{\mathscr{J}}\}$, with the support set $\bar{\mathscr{J}}$ denoted as the complement of the set $\mathscr{J}$ (index set for zero values for the Fourier transform of the probe). We will explain why it would help to remove the grid pathology intuitively. Assume that one gets a solution multiplied by a non-constant vector e, such that one gets $\mathcal{F}(w \circ S_j(u \circ e)) = (\mathcal{F}(\mathcal{S}_j e) * \mathcal{F}w) * \mathcal{F}(\mathcal{S}_j u)$. Obviously, it demonstrates that $\mathcal{F}(\mathcal{S}_j e) * \mathcal{F}w$ will enlarge the support set, that may disobey the compact support constraint.

For simplicity, we consider the blind ptychography problem for two-subdomain DD:

$$\min\nolimits_{\{w,u_1,u_2,v\}} \sum\nolimits_{d=1}^2 \mathcal{G}_\epsilon(B_d(w,u_d); f_d) + \mathbb{I}_{\mathcal{O}}(w), \quad s.t.\ \pi_{d,3-d} u_d - v = 0, d = 1, 2,$$

where the bilinear mapping $B_d(w,u_d)$ is denoted as $(B_d)_{j_d}(w,u_d) := \mathcal{F}(w\circ\left(S^d_{j_d}u_d\right))\ \forall\ 0\le j_d\le J_d-1(\sum_{d=1}^2 J_d = J)$, and the indicator function $\mathbb{I}_{\mathcal{O}}$ is defined as

$$\mathbb{I}_{\mathcal{O}}(w) := \begin{cases} 0, & \text{if } w\in\mathcal{O};\\ +\infty, & \text{otherwise.}\end{cases}$$

To enable parallel computing, we consider the following constraint optimization problems

$$\begin{aligned}&\min_{\{w,w_1,w_2,u_1,u_2,v,z_1,z_2\}}\sum_{d=1}^2\mathcal{G}_\epsilon(z_d;f_d)+\mathbb{I}_{\mathcal{O}}(w)\\ &s.t.\ \pi_{1,2}u_1-v=0,\ \ \pi_{2,1}u_2-v=0,\ w_d=w,\ z_d=B_d(w_d,u_d),d=1,2.\end{aligned}$$

To get rid of heavy notations, we introduce the following definitions. By denoting

$$\boldsymbol{\pi}=\begin{pmatrix}\pi_{1,2} & \mathbf{0}\\ 0 & \pi_{2,1}\end{pmatrix},\ \mathbf{I}_0=\begin{pmatrix}I_0\\ I_0\end{pmatrix},\ \mathbf{I}_1=\begin{pmatrix}I_1\\ I_1\end{pmatrix},\ \mathbf{B}(\mathbf{W},\mathbf{U})=\begin{pmatrix}B_1(\omega_1,u_1)\\ B_2(\omega_2,u_2)\end{pmatrix}$$

with identity matrices I_0, I_1, we rewrite the constrained condition below:

$$\boldsymbol{\pi}\mathbf{U}-\mathbf{I}_0v=0,\ \ \mathbf{W}-\mathbf{I}_1w=0,\ \ \mathbf{B}(\mathbf{W},\mathbf{U})-\mathbf{Z}=0,$$

where $\mathbf{U}=(u_1^T,u_2^T)^T,\mathbf{W}=(w_1^T,w_2^T)^T$, and $\mathbf{Z}=(z_1^T,z_2^T)^T$. Hence we consider the following model:

$$\begin{aligned}&\min_{w,\mathbf{W},\mathbf{U},v,\mathbf{Z}}\mathcal{G}_\epsilon(\mathbf{Z};\mathbf{f})+\mathbb{I}_{\mathcal{O}}(w)\\ &\text{s.t.}\ \ \boldsymbol{\pi}\mathbf{U}-\mathbf{I}_0v=0,\ \ \mathbf{W}-\mathbf{I}_1w=0,\ \ \mathbf{B}(\mathbf{W},\mathbf{U})-\mathbf{Z}=0,\end{aligned}$$

with $\mathbf{f}:=(f_1^T,f_2^T)^T$.

Similarly, the augmented Lagrangian can be formulated below:

$$\begin{aligned}&\mathcal{L}_b(w,\mathbf{W},\mathbf{U},v,\mathbf{Z},\boldsymbol{\Lambda},\boldsymbol{\Gamma},\boldsymbol{\Delta})=\mathcal{G}_\epsilon(\mathbf{Z};\mathbf{f})+\mathbb{I}_{\mathcal{O}}(w)\\ &\quad+r\Re(\langle\boldsymbol{\pi}\mathbf{U}-\mathbf{I}_0v,\boldsymbol{\Lambda}\rangle)+\eta\Re(\langle\mathbf{B}(\mathbf{W},\mathbf{U})-\mathbf{Z},\boldsymbol{\Gamma}\rangle)+\mu\Re(\langle\mathbf{W}-\mathbf{I}_1w,\boldsymbol{\Delta}\rangle)\\ &\quad+\tfrac{r}{2}\|\boldsymbol{\pi}\mathbf{U}-\mathbf{I}_0v\|^2+\tfrac{\eta}{2}\|\mathbf{B}(\mathbf{W},\mathbf{U})-\mathbf{Z}\|^2+\tfrac{\mu}{2}\|\mathbf{W}-\mathbf{I}_1w\|^2,\end{aligned}\tag{3.7}$$

with multipliers $\boldsymbol{\Lambda},\boldsymbol{\Gamma},\boldsymbol{\Delta}$ and positive parameters r,η,μ. Then alternatively one needs to solve the following saddle point problem below

$$\max_{\boldsymbol{\Lambda},\boldsymbol{\Gamma},\boldsymbol{\Delta}}\ \min_{w,\mathbf{W},\mathbf{U},v,\mathbf{Z}}\mathcal{L}_b(w,\mathbf{W},\mathbf{U},v,\mathbf{Z},\boldsymbol{\Lambda},\boldsymbol{\Gamma},\boldsymbol{\Delta}).\tag{3.8}$$

One can solve the above saddle point problem step by step using a variant ADMM with additional proximal term for the $\mathbf{U}-$subproblem below:

$$(w^{n+1},v^{n+1},\mathbf{Z}^{n+1})=\arg\min_{w,v,\mathbf{Z}}\mathcal{L}_b(w,\mathbf{W}^n,\mathbf{U}^n,v,\mathbf{Z},\boldsymbol{\Lambda}^n,\boldsymbol{\Gamma}^n,\boldsymbol{\Delta}^n)\tag{3.9}$$

$$\boldsymbol{\Gamma}^{n+1}=\boldsymbol{\Gamma}^n+\mathbf{B}(\mathbf{W}^n,\mathbf{U}^n)-\mathbf{Z}^{n+1};\tag{3.10}$$

$$\mathbf{W}^{n+1}=\arg\min_{\mathbf{W}}\mathcal{L}_b(w^{n+1},\mathbf{W},\mathbf{U}^n,v^{n+1},\mathbf{Z}^{n+1},\boldsymbol{\Lambda}^n,\boldsymbol{\Gamma}^{n+1},\boldsymbol{\Delta}^n)\tag{3.11}$$

$$\mathbf{U}^{n+1}=\arg\min_{\mathbf{U}}\mathcal{L}_b(w^{n+1},\mathbf{W}^{n+1},\mathbf{U},v^{n+1},\mathbf{Z}^{n+1},\boldsymbol{\Lambda}^n,\boldsymbol{\Gamma}^{n+1},\boldsymbol{\Delta}^n)+\tfrac{\gamma}{2}\|\mathbf{U}-\mathbf{U}^n\|^2\tag{3.12}$$

$$\boldsymbol{\Delta}^{n+1}=\boldsymbol{\Delta}^n+\mathbf{W}^{n+1}-\mathbf{I}_1w^{n+1};\tag{3.13}$$

$$\boldsymbol{\Lambda}^{n+1}=\boldsymbol{\Lambda}^n+\boldsymbol{\pi}\mathbf{U}^{n+1}-\mathbf{I}_0v^{n+1}.\tag{3.14}$$

For the $w-$subproblem, $w^{n+1}=\arg\min_w\mathbb{I}_{\mathcal{O}}(w)+\frac{\mu}{2}\|\boldsymbol{\Delta}^n+\mathbf{W}^n-\mathbf{I}_1w\|^2$. Readily one has

$$w^{n+1}=\tfrac{1}{2}\mathcal{F}^*M\mathcal{F}\mathbf{I}_1^T(\boldsymbol{\Delta}^n+\mathbf{W}^n),\tag{3.15}$$

where the matrix M is diagonal with diagonal elements defined as

$$M(j,j) = \begin{cases} 1, & \text{if } j \in \mathscr{J}; \\ 0, & \text{otherwise.} \end{cases}$$

For the $v-$subproblem,

$$v^{n+1} = \arg\min_{v} \tfrac{r}{2}\|\mathbf{\Lambda}^n + \boldsymbol{\pi}\mathbf{U}^n - \mathbf{I}_0 v\|^2 = \tfrac{1}{2}\mathbf{I}_0^T(\mathbf{\Lambda}^n + \boldsymbol{\pi}\mathbf{U}^n). \tag{3.16}$$

For the $z-$subproblem,

$$\begin{aligned} \mathbf{Z}^{n+1} &= \arg\min_{\mathbf{Z}} \mathcal{G}_\epsilon(\mathbf{Z};\mathbf{f}) + \tfrac{\eta}{2}\|\mathbf{\Gamma}^n + \mathbf{B}(\mathbf{W}^n,\mathbf{U}^n) - \mathbf{Z}\|^2 \\ &= \mathrm{Prox}_{\mathcal{G}_\epsilon,\eta}(\mathbf{\Gamma}^n + \mathbf{B}(\mathbf{W}^n,\mathbf{U}^n)), \end{aligned} \tag{3.17}$$

where $\mathrm{Prox}_{\mathcal{G}_\epsilon,\eta}(\mathbf{Z}) = (\mathrm{Prox}^T_{\mathcal{G}_\epsilon,\eta}(z_1), \mathrm{Prox}^T_{\mathcal{G}_\epsilon,\eta}(z_2))^T \ \ \forall\ \mathbf{Z} = (z_1^T, z_2^T)^T$.

Define two related operators by fixing one variable for the bilinear operator $\mathbf{B}(\cdot,\cdot)$ as $\mathbf{D}_{\mathbf{W}}(\mathbf{U}) := \mathbf{B}(\mathbf{W},\mathbf{U})$, $\mathbf{D}_{\mathbf{U}}(\mathbf{W}) := \mathbf{B}(\mathbf{W},\mathbf{U}) \ \ \forall\ \mathbf{W},\mathbf{U}$. Then $\mathbf{D}_{\mathbf{W}}$ and $\mathbf{D}_{\mathbf{U}}$ are linear, and moreover, they are linear (also bounded) w.r.t. the subscripts $\mathbf{W},\mathbf{U}$ respectively.

For $\mathbf{W}-$subproblem, one has

$$\begin{aligned} \mathbf{W}^{n+1} &= \arg\min_{\mathbf{W}} \tfrac{\eta}{2}\|\mathbf{B}(\mathbf{W},\mathbf{U}^n) - \mathbf{Z}^{n+1} + \mathbf{\Gamma}^{n+1}\|^2 + \tfrac{\mu}{2}\|\mathbf{W} - \mathbf{I}_1 w^{n+1} + \mathbf{\Delta}^n\|^2 \\ &= \big(\eta\mathbf{D}^*_{\mathbf{U}^n}\mathbf{D}_{\mathbf{U}^n} + \mu\mathbf{I}_1\big)^{-1}\big(\eta\mathbf{D}^*_{\mathbf{U}^n}(\mathbf{Z}^{n+1} - \mathbf{\Gamma}^{n+1}) + \mu(\mathbf{I}_1 w^{n+1} - \mathbf{\Delta}^n)\big), \end{aligned} \tag{3.18}$$

with $\mathbf{D}^*_{\mathbf{U}^n}\mathbf{D}_{\mathbf{U}^n} = \mathrm{diag}\Big(\big((\sum_{j_1=0}^{J_1-1}\mathcal{S}^1_{j_1}|u_1^n|^2)^T, (\sum_{j_2=0}^{J_2-1}\mathcal{S}^2_{j_2}|u_2^n|^2)^T\big)^T\Big)$.

For $\mathbf{U}-$subproblem, one has to solve the following problem

$$\begin{aligned} \mathbf{U}^{n+1} &= \arg\min_{\mathbf{U}} \tfrac{\eta}{2}\|\mathbf{B}(\mathbf{W}^{n+1},\mathbf{U}) - \mathbf{Z}^{n+1} + \mathbf{\Gamma}^{n+1}\|^2 + \tfrac{r}{2}\|\boldsymbol{\pi}\mathbf{U} - \mathbf{I}_0 v^{n+1} + \mathbf{\Lambda}^n\|^2 + \tfrac{\gamma}{2}\|\mathbf{U} - \mathbf{U}^n\|^2 \\ &= \big(\eta\mathbf{D}^*_{\mathbf{W}^{n+1}}\mathbf{D}_{\mathbf{W}^{n+1}} + r\boldsymbol{\pi}^T\boldsymbol{\pi} + \gamma\mathbf{I}\big)^{-1}\big(\eta\mathbf{D}^*_{\mathbf{W}^{n+1}}(\mathbf{Z}^{n+1} - \mathbf{\Gamma}^{n+1}) + r\boldsymbol{\pi}^T(\mathbf{I}_0 v^{n+1} - \mathbf{\Lambda}^n) + \gamma\mathbf{U}^n\big), \end{aligned} \tag{3.19}$$

where $\mathbf{D}^*_{\mathbf{W}^{n+1}}\mathbf{D}_{\mathbf{W}^{n+1}} = \mathrm{diag}\Big(\big((\sum_{j_1=0}^{J_1-1}(\mathcal{S}^1_{j_1})^T|w_1^{n+1}|^2)^T, (\sum_{j_2=0}^{J_2-1}(\mathcal{S}^2_{j_2})^T|w_2^{n+1}|^2)^T\big)^T\Big)$ and $\mathbf{I}$ denotes the identity matrix, i.e. $\mathbf{I}\mathbf{U} = \mathbf{U}$.

Finally the **o**verlapping **DD** based **b**lind **p**tychography (OD^{2}BP) is given as below:

Algorithm 3: **O**verlapping **DD** based **B**lind **P**tychography (OD^{2}BP)

Step 0. Set $n := 0$.
Step 1. Update $w^{n+1}, v^{n+1}, \mathbf{Z}^{n+1}$ in parallel by (3.15), (3.16), (3.17).
Step 2. Update the multipliers $\mathbf{\Gamma}^{n+1}$ by (3.10).
Step 3. Update $\mathbf{W}^{n+1}$ by (3.18).
Step 4. Update $\mathbf{U}^{n+1}$ by (3.19).
Step 5. Update $\mathbf{\Delta}^{n+1}$ and $\mathbf{\Lambda}^{n+1}$ by (3.13) and (3.14).
Step 6. If satisfying the stopping condition, then stop and output $\mathbf{U}^{n+1}$ as the final output; otherwise, set $n := n+1$, and go to Step 1.

For the convergence analysis, the blind case becomes more sophisticated. Limited to the current technique, we have to make the assumption of the boundedness for the iterative sequence. Then with proper (r,η,μ,γ), similarly to the nonblind case, one can prove that any limit point of $\{\widehat{X}^n\}$ converges to the stationary point of the saddle point problem (3.8).

(a) (b) (c) (d)

FIG. 3. *Ground truth of the sample with absolute part (a) and phase part (b), probe with absolute part (c) and phase part (d).*

4. Numerical Experiments. To get perfect reconstruction results, periodical boundary condition is usually enforced as [5], that produces almost same redundancy of each pixel of the sample. To make the simulation more realistic, instead we assume that the image to be recovered has boundary with pixel values being all ones, because the sample during the experiments are usually in the vacuum and the region without sample occupying has constant contrast. In the implementation of all algorithms, we enforce the region to be ones.

We consider the zone-plate probe with 64×64 pixels (See Fig. 3 (c)-(d)), and the complex-valued sample is generated by taking two real-valued images as its absolute parts (See Fig. 3 (a)) and phase (See Fig. 3 (b)) parts respectively. The raster grid is adopted for ptychography scan, i.e. all scanning points lie in isometric square grid.

For noisy free measurements, the proposed algorithms stop at the n^{th} iteration, if the R-factors $\mathrm{RF}^n := \frac{\sum_d \||A_d u_d^n| - \sqrt{f_d}\|_1}{\sum_d \|\sqrt{f_d}\|_1} \leq 1.0 \times 10^{-5}$ or $\frac{\sum_d \||B_d(w^n, u_d^n)| - \sqrt{f_d}\|_1}{\sum_d \|\sqrt{f_d}\|_1} \leq 1.0 \times 10^{-5}$ for non-blind and blind recovery, respectively, or the maximum iteration number reaches 1000. For the noisy measurements, the proposed algorithms stop at n^{th} iteration, if the relative error $\mathrm{RE}^n := \max_d \frac{\|u_d^n - u_d^{n-1}\|}{\|u_d^n\|} \leq 1.0 \times 10^{-3}$ or the maximum iteration number reaches 200. In order to measure the quality of recovery from noisy measurements, the signal-to-noise ratio (SNR) in dB is used, which is denoted below: $\mathrm{SNR}(u_r, u_g) = -10 \log_{10} \frac{\|u_r - u_g\|^2}{\|u_r\|^2}$, where u_r and u_g corresponds to the recovery image and ground truth respectively.

We initialize all variables as shown in Algorithms 1-3. As mentioned in subsection 2.2, the parameter ϵ used for the smooth truncated metric (2.7) sets to 0.5. The other parameters appearing in the proposed algorithms are chosen heuristically in order to either get faster convergence for noiseless measurements, or get better recovery quality for noisy measurements, which will be specified in the following tests. Finally, the final solution over the entire domain is obtained by merging the solutions on the subdomains derived by proposed algorithms, i.e. keeping the pixel values of non-overlapping region unchanged, while averaging the overlapping regions.

4.1. Performances of OD^{2}P. We first show the performance of the proposed OD^{2}P algorithm for the nonblind case with two-subdomain decomposition. Set the parameters $\eta = 0.1, r = 4.0 \times 10^3$. The resolution of the sample is of 256×256 pixels. Set the scan stepsize to 8 pixels for both x and y directions. Therefore the entire measurement f consists of $J = 25 \times 25$ frames, and its partitions f_1 and f_2 consist of 13×25 and 12×25 frames respectively. The width of the overlapping region is 56 (pixels). The recovery results are put in Fig. 4, where the recovery results (absolute parts in the first row of Fig. 4 and phase parts in the second row of Fig. 4) at 1st, 2nd, 5th, 50th, and the final iterations demonstrate how the proposed algorithm improve the results gradually. Especially, one may notice that the mismatch between the overlapping regions of two decomposed parts disappears as iteration goes, by inferring from the first three columns of Fig. 4. That again shows the efficiency of the proposed algorithm. The absolute values of residual between the recovery images and the truth are put in Fig. 5, where one can obviously observe the differences between two decomposed parts get weak as iteration goes. The errors changes including the relative errors and R-factors w.r.t. iteration numbers are put in Fig. 6 (a), that implies the convergence of the proposed algorithm. However, ripples appear in these curves of Fig. 6 (a). With larger $\eta = 0.2$, such ripples disappear as shown in Fig. 6 (b), while the convergence gets slower since the proposed algorithm reaches the desired error tolerance after more iterations (181 iterations). Please see more tests about the impact by the parameters in section 4.3.

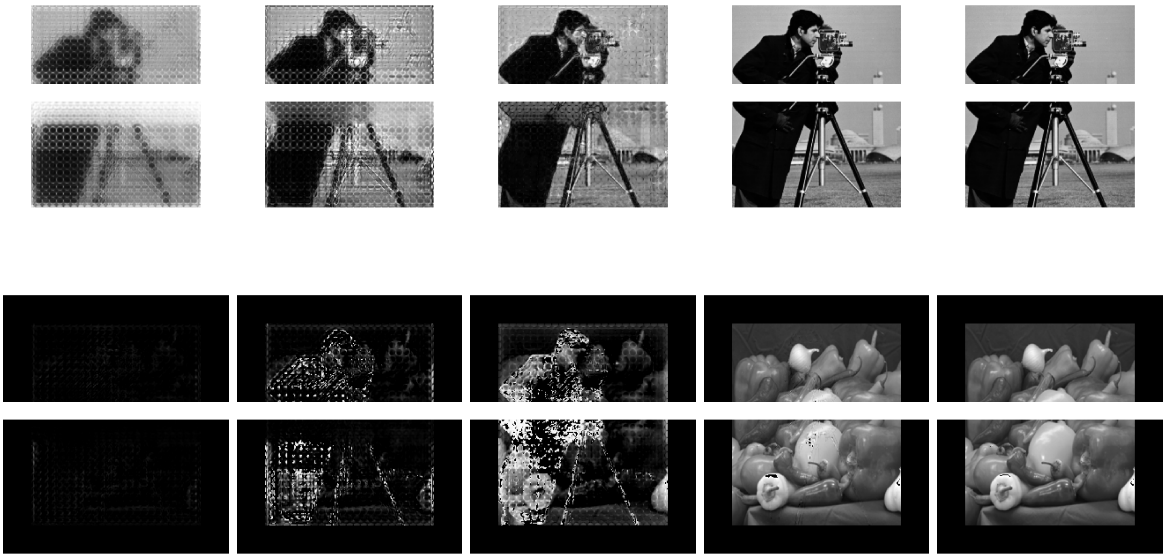

(a) 1st (b) 2nd (c) 5th (d) 50th (e) 168th

FIG. 4. *Recovery results at 1st, 2nd, 5th, 50th, 168th (final iteration) iterations. Recovered absolute parts (top and down parts for decomposed samples) in 1-2 rows and phase parts in 3-4 rows respectively (top and down parts for decomposed samples), shown in the range of* $[0, 1]$ *and* $[0, \pi]$ *for the absolute and phase parts respectively.*

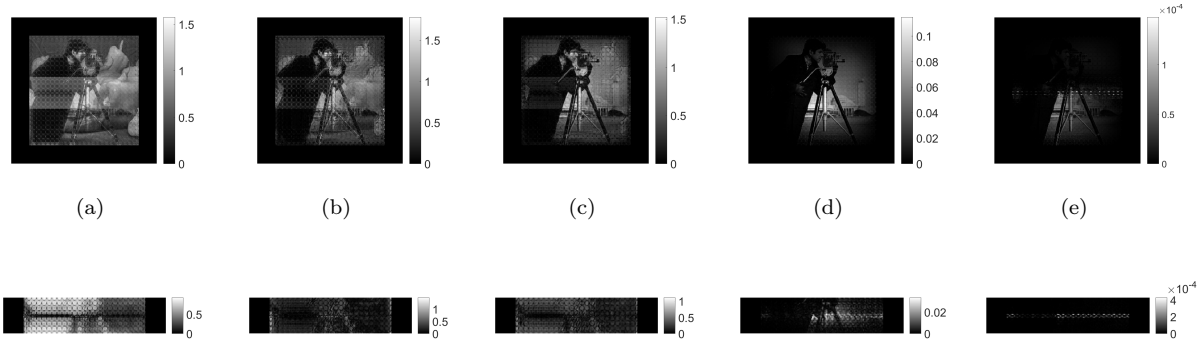

(a) (b) (c) (d) (e)

(f) (g) (h) (i) (j)

FIG. 5. *Residuals. (a)-(e): absolute values of the differences between the recovery results at 1st, 2nd, 5th, 50th, 168th (final iteration) iterations and the truth; (f)-(j): errors between the overlapping parts of two subdomains at different iterations.*

To further show the performance the proposed algorithm, the test on the noisy data is given as well. Noisy data is generated by contamination of Poisson noises with different levels (using a scaling factor to control the noise level), such that two different noisy cases with $\text{SNR}_{intensity} = 39.8, 29.9$dBs ($\text{SNR}_{intensity}$ denotes the SNR between the noisy and clean measurements) are considered. The parameter η sets to the same as the noiseless case, while r sets to 90, and 150 for two different noise levels respectively. Consider the same DD as above noiseless case. We put the recovery results in Fig. 7 (the SNRs of final recovered images are 18.1 dB and 12.2 dB). That demonstrates the proposed algorithm can work well for the Poisson noisy data, showing great potential for real experimental data analysis (usually contaminated by Poisson noise).

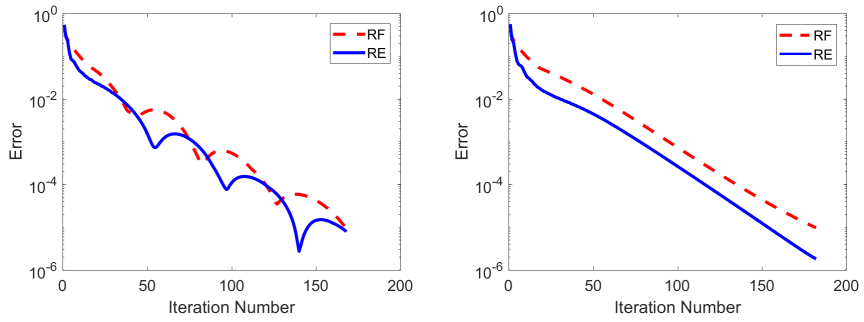

(a) (b)

FIG. 6. *RF (R-factor), and RE (Relative error) changes v.s. iterations with different η in the case of nonblind and 2-subdomain DD. Left: $\eta = 0.1, r = 4.0 \times 10^3$; Right: $\eta = 0.2, r = 4.0 \times 10^3$.*

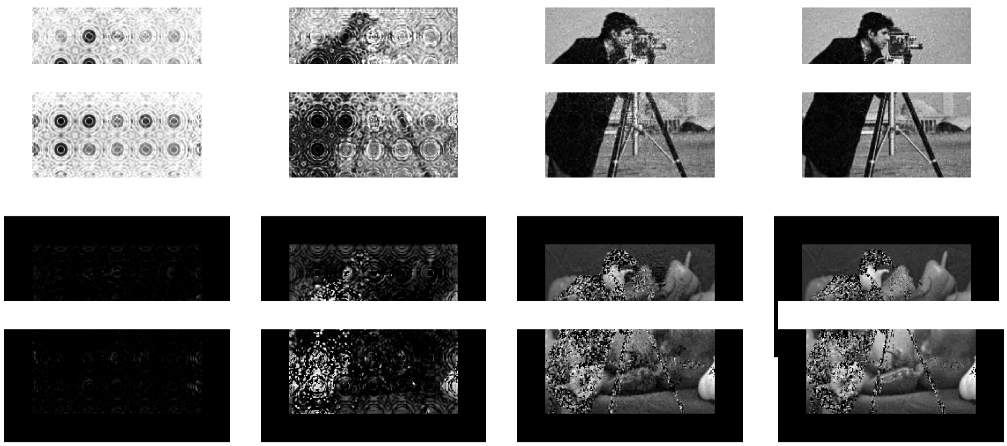

(a) 1st (b) 5th (c) 50th (d) 200th

(e) 1st (f) 5th (g) 50th (h) 200th

FIG. 7. *Recovery results from noisy measurements at 1st, 5th, 50th, 200th (final iteration) iterations. Top four rows for noisy measurements with $SNR_{intensity} = 39.8$: absolute parts (1st-2nd rows) and phase parts (3rd-4th rows) of recovered results on subdomains; Four rows below for noisy measurements with $SNR_{intensity} = 29.9$: absolute parts (5th-6th rows) and phase parts (7th-8th rows) of recovered results on subdomains. They are shown in the range of $[0, 1]$ and $[0, \pi]$ for the absolute and phase parts respectively.*

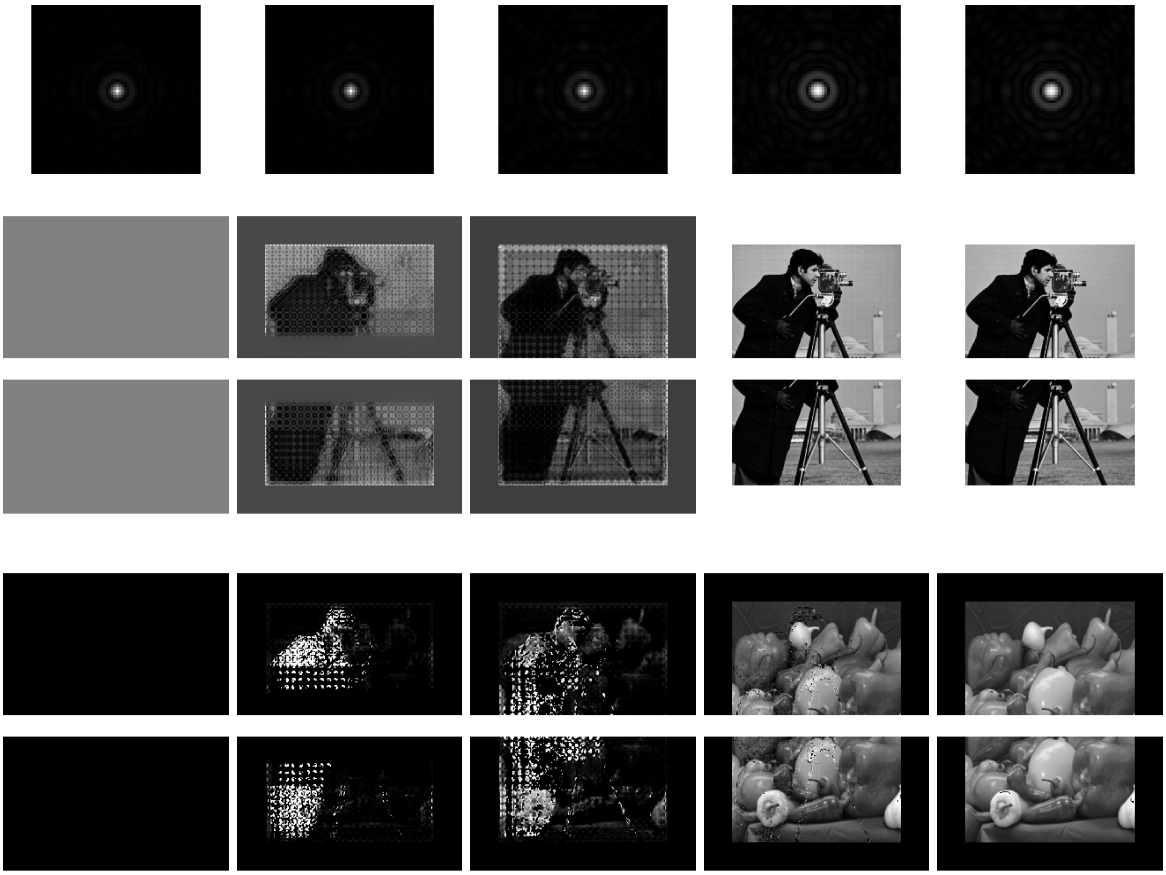

(a) 1st (b) 2nd (c) 5th (d) 50th (e) 211th

FIG. 8. *Blind recovery results at 1st, 2nd, 5th, 50th, 211th (final iteration) iterations. The first and second rows: Recovered absolute parts (top and down parts for decomposed samples) and phase parts (top and down parts for decomposed samples) respectively, shown in the range of* $[0, 1000]$, $[0, 1]$ *and* $[0, \pi]$ *for the first, 2nd-3rd, and last two rows, respectively. The parameters set to* $\eta = 0.1, r = 5.0 \times 10^3, \mu = 2.0 \times 10^2$.

4.2. Extended Tests. To further test the performances of proposed DDMs, we will test more cases, including blind recovery with two subdomains and the nonblind recovery with multiple subdomains.

(1) Blind recovery

Initial guess of the probe is generated by $w^0 := \frac{1}{J}\sum_j \mathcal{F}^* \sqrt{f_j}$ as [5]. Here we will show the performance of OD^{2}BP for the blind case with two-subdomain decomposition, where same DD is considered as section 4.1). We put the recovery results including the absolute parts of recovered probe, the absolute and phase parts of recovered images to Fig. 8 at the 1st, 2nd, 5th, 50th, and the final iterations. Similarly to the nonblind case, the mismatch between the iterative solutions on the two subdomains gradually disappears and furthermore, the probe is well recovered meanwhile, demonstrating that the proposed algorithm also works well for the blind case.

(2) Multiple subdomains

Here we will show the performance of OD^{2}P$_m$. For simplicity, the stripe-type multiple DD is implemented. To get a relative large problem, we consider the image with 512×512 pixels (Interpolated of the image shown in Fig. 3), and the scan step size sets to 16 pixels. The width of the overlapping regions is 48 (pixels). The parameters set to the same as the case of two-subdomain. We first put the recovery results in the case of 4 subdomains to Fig. 9, immediately showing the effectiveness of proposed algorithm in the case of multiple subdomains. More tests are conducted with $D = 6, 8, 10$ subdomains DD, and the related convergence curves are put to Fig. 10. On one hand, one can readily infer that the proposed algorithm

(a) 1st (b) 2nd (c) 5th (d) 50th (e) 200th

FIG. 9. *Recovery results with $D = 4$ subdomains at 1st, 2nd, 5th, 50th, 200th iterations: Recovered absolute parts (1st-4th rows) and phase parts (5th-8th rows) of the iterative solutions on the four subdomains, respectively. They are shown in the range of $[0, 1]$ and $[0, \pi]$ for the absolute and phase parts respectively.*

converges pretty well as numbers of subdomains vary. On the other hand, its convergence becomes slower as the number of subdomains increase. However, it seems not very sensitive to the number of subdomains at least up to 10 subdomains, since the maximum iteration number to reach the given accuracy changes a little bit (around 10% more iterations for 10-subdomains than that for 2-subdomain) as reported in the following Table 1.

We also measure the virtual wall-clock times (The proposed OD^{2}P$_m$ algorithm is assumed to be fully parallelized at the subdomain regardless of the communication time as [24]), and a single processor handles a single subdomain in order to show the potential of parallel computing, and report them in Table 1, that show high speedup ratios and the speedup efficiency (speedup ratios divided by the number of subdomains) is above 80%. Although we only report the virtual wall-clock time regardless of the communication cost, the proposed algorithm should be suitable for parallel computing, due to the low cost of information exchange happening on the narrow overlapping regions of adjacent subdomains. Hence, we will further evaluate the performance of proposed algorithms on large-scale computer clusters, and leave it as future work.

4.3. Impact by parameters. In order to evaluate the robustness of proposed OD^{2}P w.r.t. the parameters, we conduct the experiments with noiseless data, where one parameter varies and meanwhile other parameters are kept unchanged. Set $\eta_0 = 0.1, r_0 = 4.0 \times 10^3$. The scan stepsize sets to 8 pixels. We show the performance impacted by setting $\eta \in \{5^{-2} \times \eta_0,\ 5^{-1} \times \eta_0,\ \eta_0,\ 5 \times \eta_0,\ 5^2 \times \eta_0\}$ (keeping $r = r_0$), and put the convergence curves in Fig. 11 (a)-(b). Meanwhile, by setting $r \in \{5^{-2} \times r_0,\ 5^{-1} \times r_0,\ r_0,\ 5 \times r_0,\ 5^2 \times r_0\}$ (keeping $\eta = \eta_0$), the convergence curves are put in Fig. 11 (c)-(d). Readily one knows that too smaller

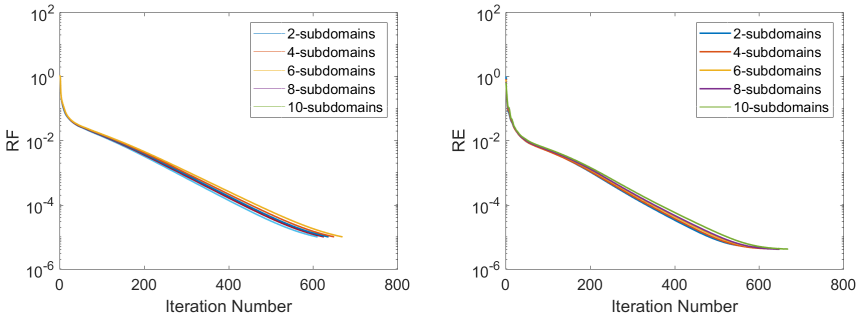

FIG. 10. *Convergence curves w.r.t. different number of subdomains: (a) RF (R-factor), and (b) RE (Relative error) changes v.s. iterations.*

TABLE 1

Performances for the case of multiple subdomains. The speedup ratio is denoted by the ratio between the virtual wall-clock time and the runtime of ADMM algorithm [5] without DD. The 2nd-3rd columns present the RF (R-factor), and RE (Relative error) for the proposed algorithms and 4th column presents the iter. no. (short for iteration number) when satisfying the stopping conditions.

D	RF(1E-5)	RE(1E-5)	Iter no.	virtual wall-clock time in seconds (Speedup ratio)
1	0.997	0.482	587	601(1.00)
2	0.995	0.458	611	346(1.74)
4	0.998	0.426	626	167(3.60)
6	0.993	0.434	637	109(5.51)
8	0.999	0.409	651	88.0(6.83)
10	0.999	0.416	670	72.0(8.35)

or bigger parameters would cause slow convergence or failure of convergence. In the future, an automatic parameter selection scheme should be developed, and we leave it as future work. The parameter impacts to other proposed algorithms seem similar to that of OD^{2}P and due to page limitation, we do not include them. Here we also remark that our convergence guarantee requires that $\eta > 1$ in order to make sure that the augmented Lagrangian of iterative sequence is lower bounded. However, in the experiments, smaller values can give faster convergences, that motivates us to get much sharper estimate of the convergence condition of the parameters, and we also leave it as future work.

5. Conclusions. Overlapping DDMs have been successfully applied to ptychography reconstruction, that lead to OD^{2}P for the two-subdomain nonblind recovery, OD^{2}P$_m$ for multiple subdomains and OD^{2}BP for the blind recovery. With the newly-designed smooth truncated metric, these proposed algorithms are efficiently computed, since all subproblems have closed form solutions, and their convergences are well guaranteed under some mild conditions. Numerical experiments are further conducted to show the performance of proposed algorithms, demonstrating good convergence speed, robust to the noise. In the future, we will optimize the current algorithms on massively parallel processing computers, and explore more other applications including Fourier ptychography [40], partial coherence analysis [4], and high dimensional ptychographic imaging problems [39].

Acknowledgments. We would like to thank the two reviewers and the associate editor for their valuable comments, which helped to improve the paper greatly. HC acknowledges support from his hosts Professors Yang Wang and James Sethian during the visits to the Dept. of Math. in Hong Kong University of Science and Technology and CAMERA in Lawrence Berkeley National Lab.

REFERENCES

[1] J. BOLTE, S. SABACH, AND M. TEBOULLE, *Proximal alternating linearized minimization for nonconvex and nonsmooth problems*, Mathematical Programming, 146 (2014), pp. 459–494.

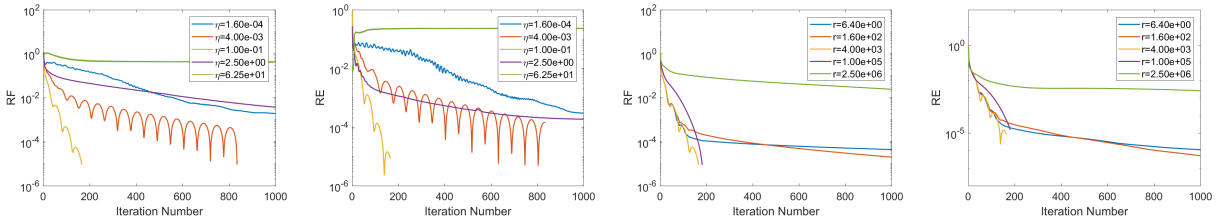

(a) (b) (c) (d)

FIG. 11. *Convergence curves w.r.t. different parameters: RF (R-factor) changes v.s. iterations with different η in (a) and different r in (c); RE (Relative error) changes v.s. iterations with different η in (b) and different r in (d);*

[2] S. Boyd, N. Parikh, E. Chu, B. Peleato, and J. Eckstein, *Distributed optimization and statistical learning via the alternating direction method of multipliers*, Found. Trends Machine learning, 3 (2011), pp. 1–122.

[3] T. F. Chan and T. P. Mathew, *Domain decomposition algorithms*, Acta numerica, 3 (1994), pp. 61–143.

[4] H. Chang, P. Enfedaque, Y. Lou, and S. Marchesini, *Partially coherent ptychography by gradient decomposition of the probe*, Acta Crystallogr., Sect. A: Found. Adv., 74 (2018), pp. 157–169.

[5] H. Chang, P. Enfedaque, and S. Marchesini, *Blind ptychographic phase retrieval via convergent alternating direction method of multipliers*, SIAM J. Imaging Sci., 12 (2019), pp. 153–185.

[6] H. Chang, Y. Lou, Y. Duan, and S. Marchesini, *Total variation–based phase retrieval for Poisson noise removal*, SIAM J. Imaging Sci., 11 (2018), pp. 24–55.

[7] H. Chang, X.-C. Tai, L.-L. Wang, and D. Yang, *Convergence rate of overlapping domain decomposition methods for the Rudin-Osher-Fatami model based on a dual formulation*, SIAM J. Image Sci., 8 (2015), pp. 564–591.

[8] H. Chang, X. Zhang, X.-C. Tai, and D. Yang, *Domain decomposition methods for nonlocal total variation image restoration*, Journal of Scientific Computing, 60 (2014), pp. 79–100.

[9] H. N. Chapman, *Phase-retrieval x-ray microscopy by wigner-distribution deconvolution*, Ultramicroscopy, 66 (1996), pp. 153–172.

[10] R. Chen, J. Huang, and X.-C. Cai, *A parallel domain decomposition algorithm for large scale image denoising*, Inverse Problems & Imaging, 13 (2019), p. 1259.

[11] P. Enfedaque, H. Chang, B. Enders, D. Shapiro, and S. Marchesini, *High performance partial coherent x-ray ptychography*, in International Conference on Computational Science, Springer, 2019, pp. 46–59.

[12] A. Fannjiang and Z. Zhang, *Fixed point analysis of Douglas-Rachford splitting for ptychography and phase retrieval*, arXiv preprint arXiv:1909.08600, (2019).

[13] M. Fornasier, A. Langer, and C.-B. Schönlieb, *A convergent overlapping domain decomposition method for total variation minimization*, Numerische Mathematik, 116 (2010), pp. 645–685.

[14] B. Gao, Y. Wang, and Z. Xu, *Solving a perturbed amplitude-based model for phase retrieval*, arXiv preprint arXiv:1904.10307, (2019).

[15] R. Glowinski and P. L. Tallec, *Augmented Lagrangian and operator-splitting methods in nonlinear mechanics*, SIAM Studies in Applied Mathematics, Society for Industrial and Applied Mathematics (SIAM), Philadelphia, PA, 1989.

[16] R. Glowinski and M. F. Wheeler, *Domain decomposition and mixed finite element methods for elliptic problems*, in First international symposium on domain decomposition methods for partial differential equations, 1988, pp. 144–172.

[17] M. Guizar-Sicairos, A. Diaz, M. Holler, M. S. Lucas, A. Menzel, R. A. Wepf, and O. Bunk, *Phase tomography from x-ray coherent diffractive imaging projections*, Optics express, 19 (2011), pp. 21345–21357.

[18] M. Guizar-Sicairos and J. R. Fienup, *Phase retrieval with transverse translation diversity: a nonlinear optimization approach*, Opt. Express, 16 (2008), pp. 7264–7278.

[19] M. Guizar-Sicairos, I. Johnson, A. Diaz, M. Holler, P. Karvinen, H.-C. Stadler, R. Dinapoli, O. Bunk, and A. Menzel, *High-throughput ptychography using eiger: scanning x-ray nano-imaging of extended regions*, Optics express, 22 (2014), pp. 14859–14870.

[20] R. Hesse, D. R. Luke, S. Sabach, and M. K. Tam, *Proximal heterogeneous block implicit-explicit method and application to blind ptychographic diffraction imaging*, SIAM J. Imaging Sci., 8 (2015), pp. 426–457.

[21] D. Jiang and H. Feng, *Domain decomposition methods for recovering Robin coefficients in elliptic and parabolic systems*, Comput. Methods Appl. Math., 18 (2018), pp. 257–274.

[22] D. Jiang, H. Feng, and J. Zou, *Overlapping domain decomposition methods for linear inverse problems*, Inverse Problems and Imaging, 9 (2015), pp. 163–188.

[23] A. Langer and F. Gaspoz, *Overlapping domain decomposition methods for total variation denoising*, SIAM Journal on Numerical Analysis, 57 (2019), pp. 1411–1444.

[24] C.-O. Lee and C. Nam, *Primal domain decomposition methods for the total variation minimization, based on dual decomposition*, SIAM Journal on Scientific Computing, 39 (2017), pp. B403–B423.

[25] C.-O. Lee, E.-H. Park, and J. Park, *A finite element approach for the dual Rudin–Osher–Fatemi model and its nonoverlapping domain decomposition methods*, SIAM Journal on Scientific Computing, 41 (2019), pp. B205–B228.

[26] P.-L. Lions, *On the Schwarz alternating method. i*, in First international symposium on domain decomposition methods for partial differential equations, vol. 1, Paris, France, 1988, p. 42.

[27] A. M. Maiden and J. M. Rodenburg, *An improved ptychographical phase retrieval algorithm for diffractive imaging*, Ultramicroscopy, 109 (2009), pp. 1256–1262.

[28] S. Marchesini, *Invited article: A unified evaluation of iterative projection algorithms for phase retrieval*, Review of

scientific instruments, 78 (2007), p. 011301.
[29] S. Marchesini, H. Krishnan, D. A. Shapiro, T. Perciano, J. A. Sethian, B. J. Daurer, and F. R. Maia, *SHARP: a distributed, GPU-based ptychographic solver*, J. Appl. Crystallogr., 49 (2016), pp. 1245–1252.
[30] S. Marchesini, Y.-C. Tu, and H.-T. Wu, *Alternating projection, ptychographic imaging and phase synchronization*, Applied and Computational Harmonic Analysis, 41 (2016).
[31] Y. S. Nashed, D. J. Vine, T. Peterka, J. Deng, R. Ross, and C. Jacobsen, *Parallel ptychographic reconstruction*, Optics express, 22 (2014), pp. 32082–32097.
[32] J. M. Rodenburg and H. M. Faulkner, *A phase retrieval algorithm for shifting illumination*, Appl. Phys. Lett., 85 (2004), pp. 4795–4797.
[33] Y. Shechtman, Y. C. Eldar, O. Cohen, H. N. Chapman, J. Miao, and M. Segev, *Phase retrieval with application to optical imaging: a contemporary overview*, Signal Processing Magazine, IEEE, 32 (2015), pp. 87–109.
[34] P. Thibault, M. Dierolf, O. Bunk, A. Menzel, and F. Pfeiffer, *Probe retrieval in ptychographic coherent diffractive imaging*, Ultramicroscopy, 109 (2009), pp. 338–343.
[35] P.-H. Tournier, I. Aliferis, M. Bonazzoli, M. de Buhan, M. Darbas, V. Dolean, F. Hecht, P. Jolivet, I. El Kanfoud, C. Migliaccio, F. Nataf, C. Pichot, and S. Semenov, *Microwave tomographic imaging of cerebrovascular accidents by using high-performance computing*, Parallel Computing, 85 (2019), pp. 88 – 97.
[36] Z. Wen, C. Yang, X. Liu, and S. Marchesini, *Alternating direction methods for classical and ptychographic phase retrieval*, Inverse Probl., 28 (2012), p. 115010.
[37] C. Wu and X.-C. Tai, *Augmented Lagrangian method, dual methods and split-Bregman iterations for ROF, vectorial TV and higher order models*, SIAM J. Imaging Sci., 3 (2010), pp. 300–339.
[38] J. Xu, X.-C. Tai, and L.-L. Wang, *A two-level domain decomposition method for image restoration*, Inverse Probl. Imaging, 4 (2010), pp. 523–545.
[39] Y.-S. Yu, M. Farmand, C. Kim, Y. Liu, C. P. Grey, F. C. Strobridge, T. Tyliszczak, R. Celestre, P. Denes, J. Joseph, H. Krishnan, F. R. N. C. Maia, A. L. D. Kilcoyne, S. Marchesini, T. P. C. Leite, T. Warwick, H. Padmore, J. Cabana, and D. A. Shapiro, *Three-dimensional localization of nanoscale battery reactions using soft x-ray tomography*, Nat. Commun., 9 (2018), p. 921.
[40] G. Zheng, R. Horstmeyer, and C. Yang, *Wide-field, high-resolution fourier ptychographic microscopy*, Nature Photonics, 7 (2013), pp. 739–745.